

# Enhancement of the Antioxidant Activity and Neurotherapeutic Features through Pyridol Addition to Tetraazamacrocyclic Molecules

Hannah M. Johnston,<sup>†</sup> Kristof Pota,<sup>†</sup> Madalyn M. Barnett,<sup>†</sup> Olivia Kinsinger,<sup>‡</sup> Paige Braden,<sup>‡</sup> Timothy M. Schwartz,<sup>†</sup> Emily Hoffer,<sup>†</sup> Nishanth Sadagopan,<sup>†</sup> Nam Nguyen,<sup>†</sup> Yu Yu,<sup>§</sup> Paulina Gonzalez,<sup>†</sup> Gyula Tircsó,<sup>||</sup> Hongli Wu,<sup>§,⊥</sup> Giridhar Akkaraju,<sup>‡</sup> Michael J. Chumley,<sup>‡</sup> and Kayla N. Green<sup>\*,†,||</sup>

<sup>†</sup>Department of Chemistry and Biochemistry and <sup>‡</sup>Department of Biology, Texas Christian University (TCU), 2950 S. Bowie, Fort Worth, Texas 76129, United States

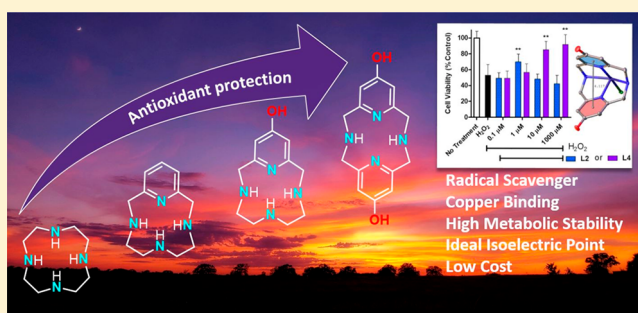
<sup>§</sup>Pharmaceutical Sciences, University of North Texas System College of Pharmacy, and <sup>⊥</sup>North Texas Eye Research Institute, University of North Texas (UNT) Health Science Center, Fort Worth, Texas 76107, United States

<sup>||</sup>Department of Inorganic and Analytical Chemistry, Faculty of Science and Technology, University of Debrecen, Egyetem tér 1, Debrecen H-4010, Hungary

## Supporting Information

**ABSTRACT:** Alzheimer's and other neurodegenerative diseases are chronic conditions affecting millions of individuals worldwide. Oxidative stress is a consistent component described in the development of many neurodegenerative diseases. Therefore, innovative strategies to develop drug candidates that overcome oxidative stress in the brain are needed. To target these challenges, a new, water-soluble 12-membered tetraaza macrocyclic pyridinophane **L4** was designed and produced using a building-block approach. Potentiometric data show that the neutral species of **L4** provides interesting zwitterionic behavior at physiological pH, akin to amino acids, and a nearly ideal isoelectric point of 7.3.

The copper(II) complex of **L4** was evaluated by X-ray diffraction and cyclic voltammetry to show the potential modes of antioxidant activity derived, which was also demonstrated by 2,2-diphenyl-1-picrylhydrazyl and coumarin carboxylic acid antioxidant assays. **L4** was shown to have dramatically enhanced antioxidant activity and increased biological compatibility compared to parent molecules reported previously. **L4** attenuated hydrogen peroxide (H<sub>2</sub>O<sub>2</sub>)-induced cell viability loss more efficiently than precursor molecules in the mouse hippocampal HT-22 cell model. **L4** also showed potent (fM) level protection against H<sub>2</sub>O<sub>2</sub> cell death in a BV2 microglial cell culture. Western blot studies indicated that **L4** enhanced the cellular antioxidant defense capacity via Nrf2 signaling activation as well. Moreover, a low-cost analysis and high metabolic stability in phase I and II models were observed. These encouraging results show how the rational design of lead compounds is a suitable strategy for the development of treatments for neurodegenerative diseases where oxidative stress plays a substantial role.



## INTRODUCTION

Alzheimer's and other neurodegenerative diseases are chronic conditions affecting millions of individuals worldwide.<sup>1,2</sup> Despite aggressive efforts, there are yet to be therapeutic agents approved for and capable of eradicating these diseases.<sup>3</sup> The deficiency of clearly understood mechanisms for the cause and progression of neurodegenerative diseases is a major impediment to developing a treatment. However, a few main themes consistently arise and are proposed to be interrelated in many of these diseases: increased oxidative stress,<sup>4–9</sup> dyshomeostasis of metal ions,<sup>10–12</sup> and protein aggregation.<sup>13–17</sup>

The human brain is particularly susceptible to protein, lipid, and DNA damage derived from the oxidative stress that occurs

when there is an imbalance between the reactive oxygen species (ROS) and the availability/activity of antioxidants.<sup>5</sup> The brain requires disproportionately large amounts of molecular oxygen for processes including cellular respiration and biosynthesis of neurotransmitters, compared to other organs of similar size. Redox-active transition-metal ions are also vital components of the brain that are essential for detoxification of free radicals, electron- and oxygen-transport processes, neurotransmitter biosynthesis, and neuronal signaling. These processes are elegantly facilitated through metal uptake and transport mechanisms as well as metal coordination

**Received:** October 2, 2019

in protein scaffolds or cofactors.<sup>18</sup> However, disruption of these systems is linked to the increased production of ROS. Unregulated redox-active metals, like copper and iron, can readily react with molecular oxygen and biological reductants such as ascorbate to produce excess ROS via Fenton- and Haber–Weiss-type reactions.<sup>19</sup> Aberrant metal ions promote  $\beta$ -amyloid ( $A\beta$ ) aggregation, a causative agent in Alzheimer's disease. Disproportionately high levels of metal ions have been observed in the hallmark  $A\beta$  plaques, are known to promote peptide aggregation, and provide an environment that also promotes the redox-active environment responsible for ROS production.<sup>10,12,14,20–22</sup> The relationship between disease causation and the progression of metal-ion misregulation, oxidative stress, and protein deposition is a challenge to untangle.<sup>10,23</sup> This work aims to focus on the development of a new, potent small molecule that targets two legs of the “piano stool” (Figure 1a) that contribute to neurodegenerative disease: oxidative stress and metal-ion misregulation.

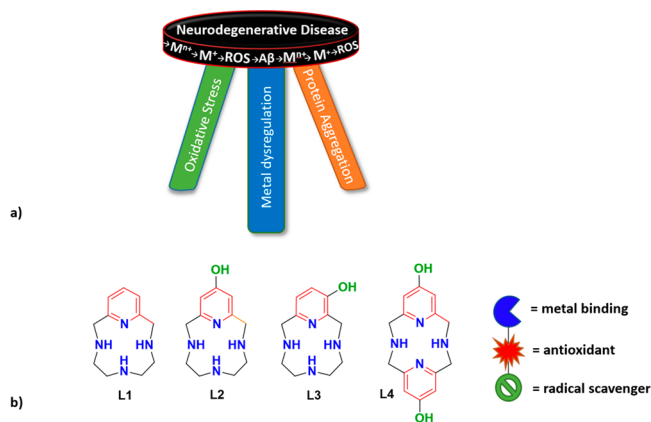


**Figure 1.** (a) Causative agents for neurodegenerative diseases and (b) structures of L1–L4 and reactivities observed to date.

Pyridinophane molecules based on L1 (Figure 1b) have been used as metal-binding scaffolds that support a range of catalytic reactions and serve as the backbone for potential magnetic resonance imaging contrast agents.<sup>24–49</sup> We have also reported applications of 12-membered pyridinophane molecules L1–L3 (Figure 1b) as potential therapeutics for neurodegenerative diseases derived from oxidative stress.<sup>50,51</sup> Such work inspired the synthesis and exploration of the new water-soluble, more-active, and biologically compatible system L4 described herein.

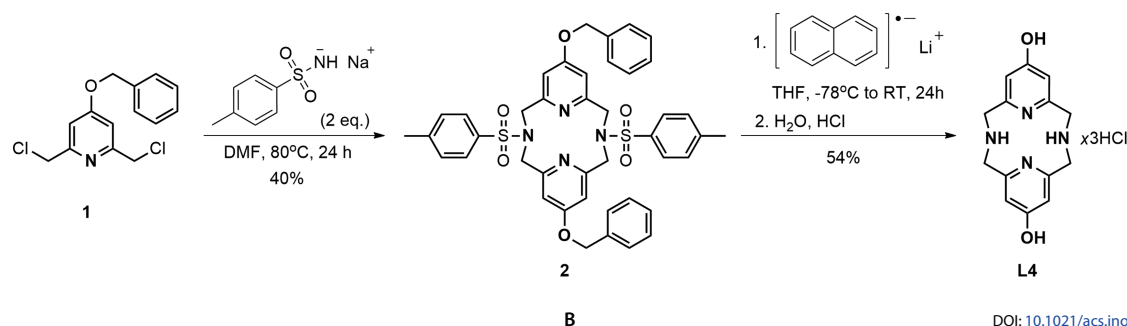
With the goal of increasing the potency and thus lowering the effective dosage, it was hypothesized that doubling the pyridol moieties of L2, while retaining the macrocycle size and

number of donor atoms, would result in an increase of the radical scavenging ability and antioxidant activity, as well as improve on the isoelectric point compared to other antioxidant macrocycles reported to date.<sup>52</sup> The design of the new molecule (L4) would preserve the water solubility, metabolic stability, and redox control of metal ions. While the  $Py_2N_2$  family of molecules based on the 2,11-diaza[3,3](2,6)-pyridinophane ligand have been explored extensively for catalytic reactions, the bispyridol L4 congener is reported here for the first time.<sup>25,27,29,32,33,41</sup> Potentiometric titrations were performed with L4 to determine the  $pK_a$  and  $pI$  values, which were compared to precursor molecules. Coumarin carboxylic acid (CCA) and 2,2-diphenyl-1-picrylhydrazyl radical (DPPH $\cdot$ ) assays were used to preliminarily evaluate the antioxidant capabilities of L4. In addition to these assays, L4 has been coordinated to copper(II), which has been associated with the development of Alzheimer's disease.<sup>53–60</sup> The CuL4 complex was characterized using X-ray diffraction (XRD) and cyclic voltammetry (CV). HT-22 cellular studies indicate that L4 is a superior antioxidant to L2, and the NRF2 pathway was upregulated to give rise to cell protection. Potent protection against hydrogen peroxide ( $H_2O_2$ )-induced cell death was also observed in a BV microglial cell (MGC) culture. These measurements, metabolism (phases I and II), cell toxicity, and other antioxidant studies encourage further exploration of L4 as well as other derivations of pyridinophanes as antioxidant therapeutic agents for neurodegenerative diseases.

## RESULTS AND DISCUSSION

**Synthesis of L4.** The synthesis of L4 was achieved via a 1:1 condensation reaction (Scheme 1). A total of 2 equiv of tosylamide monosodium salt (TsNHNa)<sup>61–64</sup> was combined with 4-benzyloxy-2,6-bis(chloromethyl)pyridine (1)<sup>50,65</sup> in *N,N*-dimethylformamide (DMF) under reflux to produce the cyclized and tosyl-protected product 8,17-benzyloxy-4,13-bis(*p*-toluenesulfonyl)-1,4,11,13-tetraazabis(2,6-pyridinophane) (2). This cyclization reaction can be visualized as proceeding through a monoalkylated intermediate followed by self-condensation in the presence of excess TsNHNa, which acts as a base, to yield the desired macrocyclic product (Scheme S1).<sup>63</sup> A low-quality solid-state structure of 2 obtained through XRD analysis (Figures S1 and S2) is observed in the lowest-energy syn chair–chair conformation. Concomitant removal of the benzyl and tosyl protecting groups was accomplished with a naphthalene-catalyzed lithiation (Scheme 1).<sup>66,67</sup> The reaction mixture was then hydrolyzed and an acidic workup yielded L4 as the trihydrochloride salt. NMR analysis was consistent with the

### Scheme 1. Synthetic Methods Used To Produce L4



connectivity shown in Scheme 1. The acid form of the ligand is highly soluble in water.

**Protonation Constants of L4.** Pharmacological behaviors, solubility, permeability,  $\log D$ , and oral absorption can be predicted or explained by taking into account the protonation state of a complex at biological pH. These factors are strongly modulated by the distribution of neutral and charged species for a selected compound. Therefore, the stepwise protonation constants ( $\log K_i^H$ ) of L4 were determined by pH-potentiometric titrations at constant ionic strength and temperature ( $I = 0.15$  M NaCl and  $T = 298$  K). The results are compiled in Table 1, along with the protonation constants

**Table 1. Protonation Constants<sup>a</sup> ( $pK_a$ ) and  $pI$  Values of Studied Cyclen and Pyridinophanes L1, L2, and L4 ( $I = 0.15$  M NaCl and  $T = 298$  K)**

	cyclen <sup>b</sup>	L1 <sup>c</sup>	L2 <sup>c</sup>	L4
$\log K_1^H$	10.66	11.37	11.56	11.307(8)
$\log K_2^H$	9.69	8.22	9.05	9.35(2)
$\log K_3^H$	1.41	1.61	5.45	5.25(3)
$\log K_4^H$			1.68	4.21(3)
$\log K_5^H$				0.98(2)
$\sum \log K_i^H$	21.76	21.20	27.74	31.10
$pI$	>10.66	>11.37	10.31	7.30

<sup>a</sup>Defined as  $K_i^H = [H_iL^{i+}]/([H^+][H_{i-1}L^{(i-1)+}])$  for  $i = 1-5$ .  
<sup>b</sup>Reference 68 ( $I = 0.15$  M NaClO<sub>4</sub>).  
<sup>c</sup>Reference 52.

previously reported for cyclen and L1 and L2.<sup>52,69-71</sup> A thorough comparison of the impact of the position of -OH on  $pK_a$  (L2 vs L3) is reported elsewhere.<sup>52</sup> For each macrocycle compared here, all N atoms are expected to undergo protonation equilibria but may not be measurable in the window of the potentiometric experiment. Furthermore, ligands L2 and L4 also contain hydroxyl groups on the 4 position of the pyridine ring also capable of protonation equilibria.

Five protonation constants were measured for L4 (Table 1) within the window of the experiment. With the addition of each pyridol moiety (L1 < L2 < L4), the ligands exhibit an increase in the values measured for the second protonation step.<sup>52</sup> This indicates that the presence of an -OH group on the pyridine ring increases the basicity of the ligand, which is consistent with the enhanced resonance stabilization imparted by the electron-donating -OH moiety on the 4 position of the pyridine ring.<sup>52</sup>

The results indicate that at pH 7.3 the  $[H_2(L4)]$  species will dominate at 98%. In fact, this neutral species is modeled to be >50% between pH values of ~6 and 9, an unusually broad range (Figure 2). Moreover, the isoelectric point of L4 ( $pI = 7.3$ ) is ideal for drug candidates.<sup>72-74</sup> This is an improvement over L2 with  $pI = 10.31$  and shows another advantage of using the additional pyridol moiety of L4 to tune pharmacological features of a potential drug.<sup>75</sup> The  $pI$  value is consistent with the water solubility observed and indicates that L4 could exhibit positive pharmaceutical properties. To gain more insight into the most stable resonance structure of L4 at physiological pH, <sup>1</sup>H NMR spectroscopy and UV spectrophotometric titrations were carried out. Elemental analysis indicated that L4 was isolated as the trihydrochloride salt, which provided a starting point for assigning the protonation sequence. Five  $pK_a$  values were observed. Therefore, the dianionic form was the most deprotonated

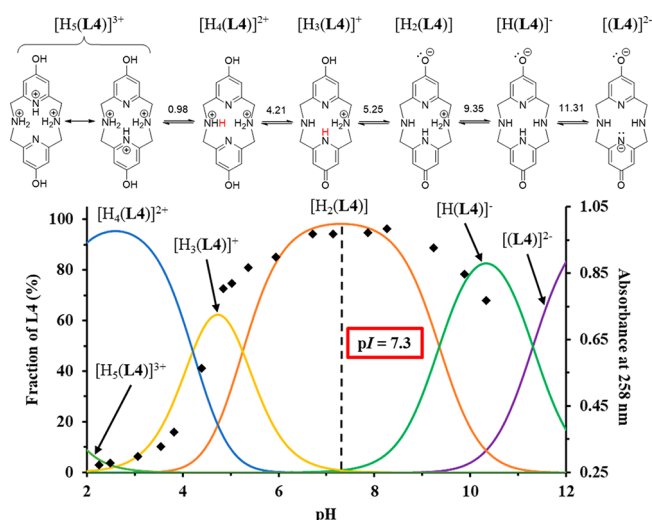


**Figure 2.** Proposed protonation sequence and equilibrium distribution diagram with absorbance values at 258 nm from UV spectrophotometric titration for L4 ( $c_L = 0.02$  mM,  $I = 0.15$  M NaCl, and  $T = 298$  K).

species detectable in the experimental window. The presence of two aromatic downfield resonances suggested an asymmetric form of L4 with negative charges on one of the pyridol O atoms and the N atom of the other pyridol moiety (Figure 2, top). The most stable resonance structure of  $[(L4)]^{2-}$  would contain both enol and keto functionalities opposite to one another. The second protonation step ( $pK_a = 9.35$ ) is assigned to a secondary amine, based on the observed upfield shifts to the aliphatic derived H atoms and no change in the downfield resonances. The third protonation event gives rise to significant changes in both the most downfield aliphatic (red squares) and aromatic (dark-blue circles) proton resonances of L4 (Figure 3), consistent with protonation of the enol group.

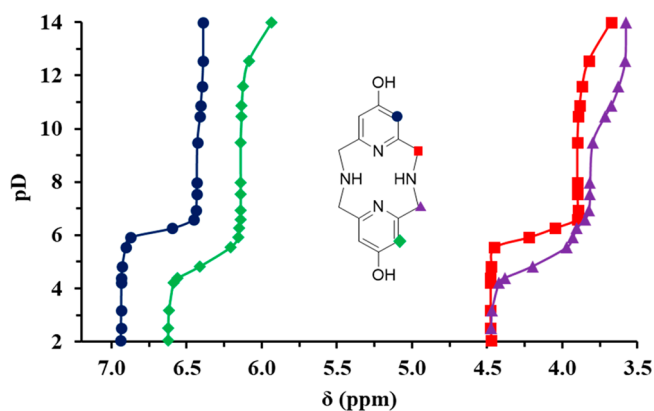


**Figure 3.** <sup>1</sup>H NMR titration curves of L4.

The small decrease in the UV-vis spectrum indicates that no large changes in the electronic structure occurred at this protonation step. However, the next protonation ( $pK_a = 4.21$ ) yields a significant decrease in the aromatic band of L4 (258 nm) concomitant with similar downfield shifts in the adjacent aromatic (green diamonds) and aliphatic (purple triangles) resonances compared to those observed with the previous protonation event. These observations are consistent with transitioning from an 8-electron/7-centered system (keto) to an aromatic 6-electron/6-centered system (enol). Only one

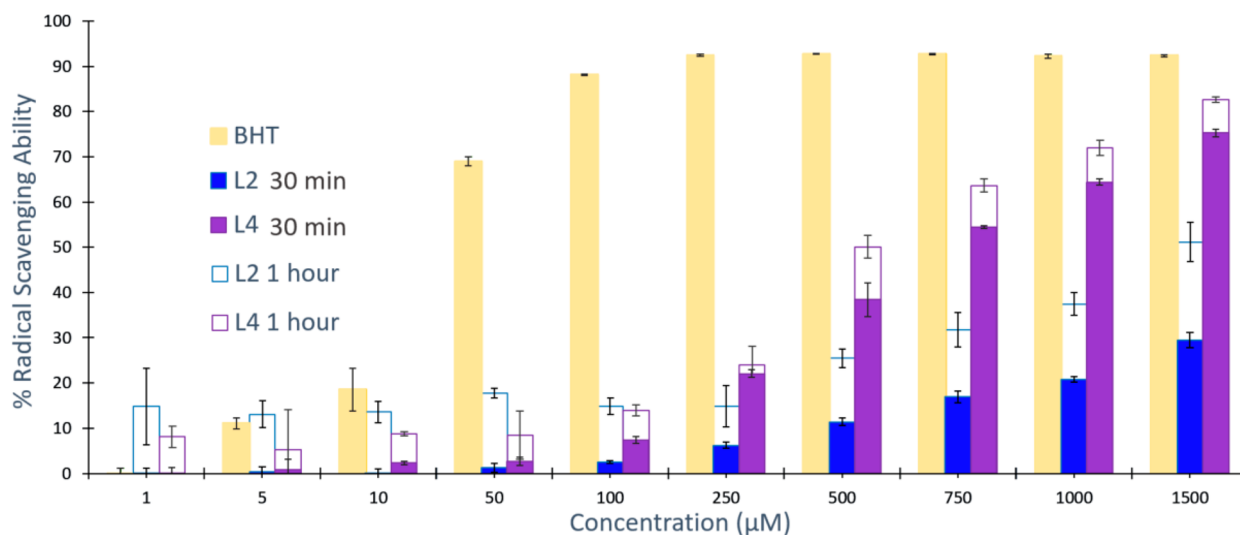


**Figure 4.** Radical scavenging ability measured using DPPH<sup>•</sup> versus L2 and L4 compared to the standard antioxidant BHT ( $n = 3$ ). The results have been standardized against DPPH<sup>•</sup> with no radical scavenger present (100%).

aliphatic resonance is observed at pH values below  $pD = 3$ . This can be explained by rearrangement of the proton (red, Figure 3, top) from the pyridine N atom to the remaining unprotonated secondary amine. The last protonation step modeled from the potentiometric data was not observable under the conditions used in the UV or NMR studies. However, further acidification of a sample of L4 resulted in only two resonances in the <sup>1</sup>H NMR spectrum (Figure S3). The symmetric bisenol form of L4 is consistent with the last acidic equivalent residing equally between the two pyridine N atoms of  $[H_5(L4)]^{3+}$ , which agrees with previously reported assignments of pyridinophanes.<sup>52,76</sup> These results highlight the need to carefully study the protonation events and indicate that the  $[H_2L4]$  species would be observed as a highly asymmetric species at physiological pH, which parallels the zwitterionic behavior of amino acids. This is in contrast to the symmetric trihydrochloride version in which it is isolated.

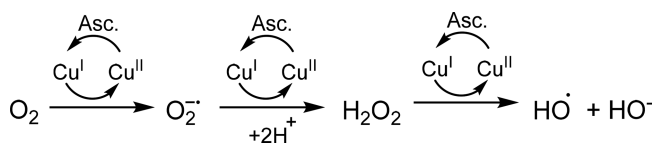
**Radical Scavenging Ability.** The strong correlation between uncontrolled oxidative stress and the development of neurodegenerative diseases has led to the study of a range of antioxidant small molecules and was the premise for the exploration of L4.<sup>77</sup> DPPH<sup>•</sup> ( $\lambda_{max} = 520$  nm) was used to assay the radical scavenging activity of L4 compared to L2.<sup>78–81</sup> A radical scavenging molecule can quench DPPH<sup>•</sup>, and the corresponding color change from purple to clear yellow can be monitored spectrophotometrically to evaluate the radical reactivity (Scheme S2).<sup>78–81</sup> The concentrations of L2 (one pyridol moiety) and L4 (two pyridol moieties) were studied over the range of 1–1500  $\mu$ M (Figure 4). 2,6-Di-*tert*-butyl-4-methylphenol, or butylated hydroxytoluene (BHT), was used as a positive control and resulted in a rapid decrease in the DPPH<sup>•</sup> absorbance band.<sup>78,79</sup> Likewise, L4 showed a strong, concentration-dependent antioxidant response beginning at 100  $\mu$ M (Figure 4). The lack of radical scavenging activity exhibited by L1 was previously shown and confirms that the pyridol moiety is responsible for the strong response exhibited with L2 and L4.<sup>50</sup> The reactivities of L2 and L4 were also tested with 2,2'-azino bis(3-ethylbenzothiazoline)-6-sulfonic acid (ABTS), but little to no reactivity was observed. This suggests that the radical scavenging activity is divergent from molecules reported by others for the potential treatment of

neurodegenerative disorders.<sup>82–84</sup> Selective reactivity with either ABTS or DPPH<sup>•</sup> has been observed for other antioxidant molecules but remains a topic of debate regarding mechanistic pathways.<sup>85–90</sup> Nevertheless, the percentage of DPPH<sup>•</sup> quenched by L4 is consistently >50% more than that of L2 and strongly supports the hypothesis that doubling the number of pyridol groups from L2 would drastically increase the radical scavenging activity.

#### Prevention of ROS Generation via Redox Cycling.

ROS can be produced by the redox cycling of redox-active transition-metal ions.<sup>79</sup> The overproduction of ROS is hypothesized to lead to the development of neurodegenerative diseases.<sup>91–94</sup> A good model for such redox cycling in the brain is the copper/ascorbate redox system (Scheme 2).<sup>50,95,96</sup> The

#### Scheme 2. Copper(II)/Copper(I) Redox Cycling Occurring in the Presence of Oxygen and Ascorbate To Produce ROS



hydroxyl radicals generated by copper(II) in the presence of ascorbate and oxygen stoichiometrically convert CCA to the fluorescent hydroxy-CCA species (Figure 5, inset).<sup>95,96</sup> Metal-ion redox chemistry is known to be modulated by coordination to strongly donating small molecules.<sup>19,97</sup> Therefore, this model system was used to evaluate the capacity of L4 to halt metal-ion redox cycling under these conditions. The results are compared to L2 to determine if the number of pyridol moieties may play a role in this reactivity as well.

The addition of 1 equiv of L4 [vs copper(II) concentration] resulted in an almost complete inhibition of CCA conversion to fluorescent hydroxy-CCA. To show the stoichiometric nature of this response, 0.5 equiv of each metal-binding molecule was added in a follow-up study. The fluorescent signal observed was greater than the samples incubated with 1 equiv but less than 50% of that compared to the sample sans a metal-binding molecule.

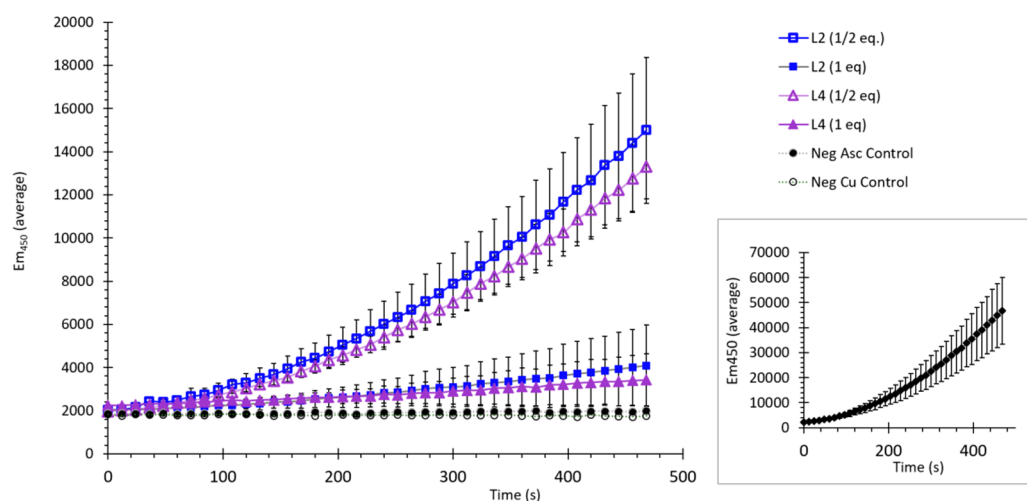


**Figure 5.** Fluorescence intensity of 7-hydroxy-CCA after incubation of CCA (100  $\mu\text{M}$ ) and ascorbate (300  $\mu\text{M}$ ) with copper(II) (10  $\mu\text{M}$ ). Compounds **L2** (0.5 equiv = 5  $\mu\text{M}$ ; 1 equiv = 10  $\mu\text{M}$ ) and **L4** (0.5 equiv = 5  $\mu\text{M}$ ; 1 equiv = 10  $\mu\text{M}$ ) were combined prior to the addition of ascorbate. No fluorescence was observed with CCA coincubated with samples of (1) ascorbate (300  $\mu\text{M}$ ) only or (2) copper(II) (10  $\mu\text{M}$ ). All solutions except  $\text{CuSO}_4 \cdot 6\text{H}_2\text{O}$  (Milli-Q water only) were dissolved and diluted in a pH = 7.4 1X  $\text{KH}_2\text{PO}_4/\text{NaCl}$  buffer containing Desferal (1  $\mu\text{M}$ ). Final volume = 3 mL ( $n = 3$ ). The inset shows the response of CCA with no metal-binding agent added.

This prevention of  $\text{OH}^\bullet$  formation was hypothesized to be a result of the molecule's ability to accommodate copper(II) but not copper(I) because of its rigidity. To test this, the open-chain, NNN-pincer 2,6-bis[(diethylamino)methyl]pyridine was produced using methods described by Vedernikov et al. and subsequently evaluated with CCA assay.<sup>98</sup> One full equivalent of the open-chain system, with respect to the copper(II) concentration, failed to give any indication of the prevention of copper redox cycling and the formation of  $\text{OH}^\bullet$  (Figure S6). This is consistent with pincer-type ligands that readily accommodate  $\text{Cu}^{\text{I}}$  ions. Furthermore, electrochemical analysis of the **CuL4** complex shows one irreversible reduction at very negative potential values ( $E_{\text{pc}} = -816$  mV vs  $\text{Fc}^+/\text{Fc}$  in DMF; Figure S7). The position of the copper(II) to copper(I) reduction is significantly more negative than that of the copper(II/I)/ascorbate reaction, thus indicating that the macrocycle stabilized the copper(II) species. Therefore, the activity observed with macrocycles to date, including **L4**, is a result of the rigidity of the macrocycle preventing the preferred geometric environment for copper(I). The lack of fluorescence observed within the CCA/copper/ascorbate system is hence attributed to the chelation of  $\text{Cu}^{\text{II}}$  ions by **L4**.

Interestingly, **L4** is slightly more efficient compared to **L2** for the prevention of hydroxyl-CCA formation. The enhanced ability of **L4** to halt redox cycling is attributed to the additional pyridol moiety, which may quench any hydroxyl radicals produced by copper(II) before interaction with the metal-binding molecules. Most importantly, both **L2** and **L4** exhibit the ability to halt the redox cycling of copper(II) and ascorbate in an aerobic environment, making molecules of this type good candidates for use as antioxidant therapeutics.

**Copper(II)-Binding Studies.** The results of **L4** with CCA assay and CV suggest that **L4** is an effective metal-binding small molecule.  $\text{Py}_2\text{N}_2$  systems have been studied extensively with metals such as manganese(II) and manganese(III) but have not been explored with copper(II) or compared with congeners like **L1** and **L2**.<sup>32,33,41,49</sup> Therefore, the copper complex of **L4** was produced and evaluated by XRD analysis. A total of 1 equiv of copper(II) perchlorate was added dropwise to a solution of **L4** at pH  $\sim 5$  (Figure 6a). The aqueous

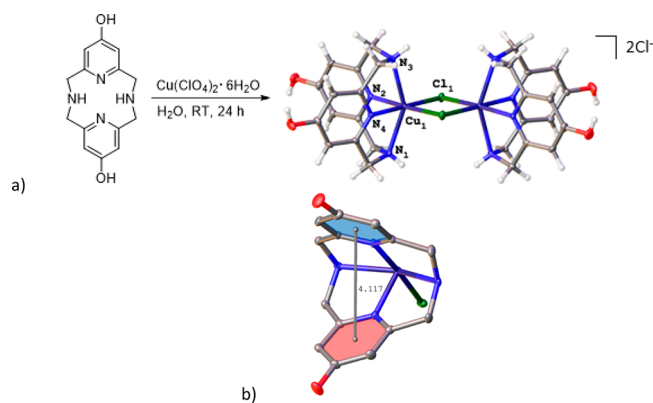


**Figure 6.** (a) Complexation reaction of **L4** with copper(II) and the resulting molecular structure of **CuL4** with an atom-labeling scheme and counterions removed for clarity. (b) Molecular structure of the monomeric unit of **CuL4** highlighting the interactions between the aromatic groups.

solution of **L4** changed from pale yellow to light blue upon the addition of copper(II). Light-green crystalline material suitable for XRD analysis was obtained by several cycles of slow evaporation of methanol (MeOH) solutions. The resulting molecular structure (Figure 6b) modeled in the  $P2_1/c$  space group shows a molecular formula of  $[\text{CuL4Cl}]_2[\text{Cl}]_2$  for the copper(II) complex of **L4** in the solid state. Each **L4** molecule binds to a  $\text{Cu}^{\text{II}}$  ion in a syn boat–boat fashion (Figure S1), with the two pyridine N atoms in the equatorial plane and the remaining two secondary N atoms in the axial plane. Hence, **L4** generates a 5–5–5–5 ring structure when bound to the  $\text{Cu}^{\text{II}}$  center. The coordination environment of each **CuL4** monomeric unit is completed by two  $\mu\text{-Cl}$  ions bridging between the  $\text{Cu}^{\text{II}}$  centers.

The *cis- $\alpha$*  coordination generated by the 12-membered pyridinophane macrocycle is consistent with the precursors in the literature.<sup>99</sup> However, the dimeric structure is unique for this copper complex. We hypothesize that the dimeric structure is a result of the highly symmetric nature of the complex in the solid state and have no evidence that it persists

in solution. The monomeric form is expected to be produced upon dissolution, particularly in coordinating solvents such as water. This assignment is supported by the monomeric species  $[\text{CuL4Cl}]^+$  observed in the mass spectrometry (MS) spectrum of **CuL4** (Figure S8). The *cis- $\alpha$*  coordination orients the pyridol rings within **L4** to potentially interact with one another. In fact, the distance between the pyridol ring centroids is 4.117 Å (Figure 6), and the angle between the rings ( $62.36^\circ$ ) is within the parameters for an edge-to-face  $\pi$ - $\pi$  interaction, which are defined as interactions between two aromatic rings in which the angle between the ring planes is between  $60^\circ$  and  $120^\circ$  and the distance between the ring centroids is less than 5.5 Å. Altogether, the coordination chemistry of **CuL4** is consistent with the results of CCA assay, which indicates a stable copper(II)-**L4** interaction with a typical bonding arrangement for the pyridinophane-type molecules.

**Therapeutic Window of L4.** Cell toxicity studies were carried out to evaluate the potential for **L4** to serve as a therapeutic agent and to establish a therapeutic window for future *in vivo* studies. HT-22 hippocampal neuronal cells were used as a model, and an  $\text{IC}_{50}$  value of  $566.4 \mu\text{M}$  was observed for **L4**. The toxicity of **L4** was compared to those of **L1**, **L2**, and cyclen (Figure 7). The order of toxicity within the series is

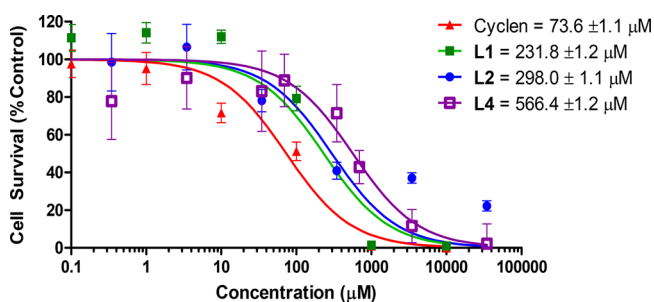


**Figure 7.** (a) Cell survival versus logarithmic concentration of HT-22 cells dosed with cyclen, **L1**, **L2**, and **L4** between  $0.1 \mu\text{M}$  to  $32 \text{ mM}$ . The data for cyclen, **L1**, and **L2** are from ref 75.

$\text{L4} < \text{L2} < \text{L1} < \text{cyclen}$ , suggesting that the bispyridol structure is well-tolerated in biological models. As noted previously, incorporation of the pyridol moiety modulates the basicity of the ligand and *pI*. Therefore, it is interesting to note that the

order of toxicity parallels that of the *pI* (Table 1) of each complex, suggesting that this feature may play a role as well. However, the correlation between *pI* and toxicity would need to be further explored in future work to validate this.

#### Antioxidant Protection in Neuronal Cells and MGCs.

To investigate the cytoprotective effects of **L4**, HT-22 cells (neuronal) were pretreated with or without **L4** ( $0.1$ – $100 \mu\text{M}$ ) for 24 h, followed by the addition of  $600 \mu\text{M}$   $\text{H}_2\text{O}_2$  for 4 h. As shown in Figure 8,  $\text{H}_2\text{O}_2$  treatment alone caused approximately 50% cell viability loss in HT-22 cells. For comparison, pretreatment with  $1 \mu\text{M}$  **L2** increased the cell viability to  $70.1 \pm 9.8\%$  (mean  $\pm$  SD,  $n = 6$ , and  $P < 0.01$ ). However, other concentrations of **L2**, including  $0.1$ ,  $10$ , and  $100 \mu\text{M}$ , did not improve the cell viability in HT-22 cells. In contrast, **L4** pretreatment could protect cells from oxidative-stress-induced cell damage in a dose-dependent manner. The HT-22 cell viability increased significantly in the  $1$ – $100 \mu\text{M}$  **L4** dose range. More than 90% cell viability was restored with **L4** pretreatment at  $100 \mu\text{M}$ , the greatest protection observed in the range studied. These cell viability assays are consistent with cell toxicity studies, which indicated that **L4** provided a broader therapeutic window as well.

To investigate the mechanism of the cytoprotective effects of **L2** and **L4**, the expression level of the nuclear factor (erythroid-derived-2)-like 2 (Nrf2) was examined by Western blot. As a transcription factor, Nrf2 plays a critical role in the regulation of a comprehensive and protective antioxidant response. When properly activated, Nrf2 translocates into the nucleus, where it binds to the antioxidant response element and promotes the expression of antioxidant enzymes. Our earlier work has shown that **L2** could activate the Nrf2 pathway in the human blood–brain barrier CMEC/D3 cells.<sup>1</sup> To investigate whether **L4** also activates Nrf2 and how this compared to **L2**, the HT-22 cells were treated for 24 h with  $1 \mu\text{M}$  **L2** and  $100 \mu\text{M}$  **L4** and the concentrations observed to provide the highest protection against  $\text{H}_2\text{O}_2$ -induced cell death for 24 h described in the studies above. Both **L2** and **L4** significantly increase the expression level of Nrf2 (Figure 8B). Collectively, the data indicate that **L2** and **L4** protect neuronal cells from oxidative-stress-induced cell damage. The neuroprotective effects of **L2** and **L4** may mediate, at least in part, through Nrf2 pathway activation as well.

Next, immortalized BV2 MGCs from C57BL/6J mouse brain tissue were used to assess the ability of **L4** compared to

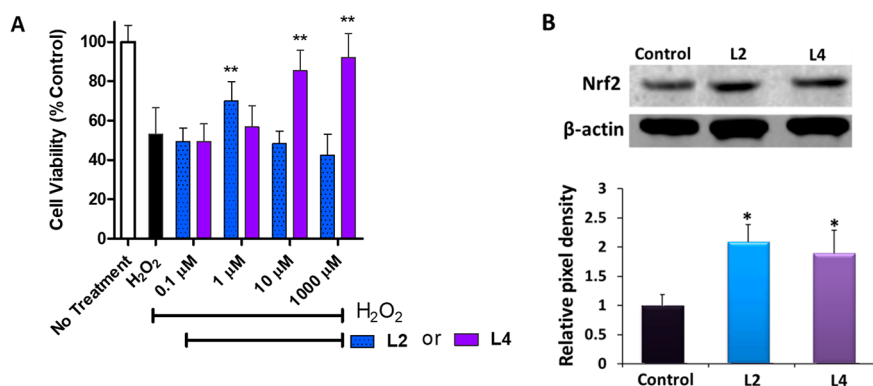


**Figure 8.** Cytoprotective effects of **L2** and **L4** in HT-22 cells. (A) HT-22 cells pretreated with  $0.1$ – $100 \mu\text{M}$  **L2** and  $0.1$ – $100 \mu\text{M}$  **L4** for 24 h and then incubated with  $600 \mu\text{M}$   $\text{H}_2\text{O}_2$  for an additional 4 h. The cell viability was measured with WST-8 assay and represented by mean  $\pm$  SD: (\*\*\*)  $P < 0.01$  and (\*\*\*)  $P < 0.001$  compared with the  $\text{H}_2\text{O}_2$ -only group ( $n = 6$ ). (B) Top panel: HT-22 cells treated with  $1 \mu\text{M}$  **L2** and  $100 \mu\text{M}$  **L4** for 24 h. Bottom panel: Relative pixel density of Nrf2 over loading control ( $\beta$ -actin): (\*)  $P < 0.05$  compared with the control ( $n = 3$ ).

L2 to provide protection from oxidative stress. MGCs work as macrophages in the brain, and their activation occurs through inflammation pathways in response to the development of A $\beta$  plaques.<sup>100,101</sup> In vitro studies indicate that stimulated MGCs phagocytose accumulated A $\beta$  and increase levels of neurotoxins in the brain.<sup>102,103</sup> Given this relationship, BV2 MGCs were used as a model as well. A decrease in the cell viability to 44% was observed with the addition of H<sub>2</sub>O<sub>2</sub> (Figure 9),

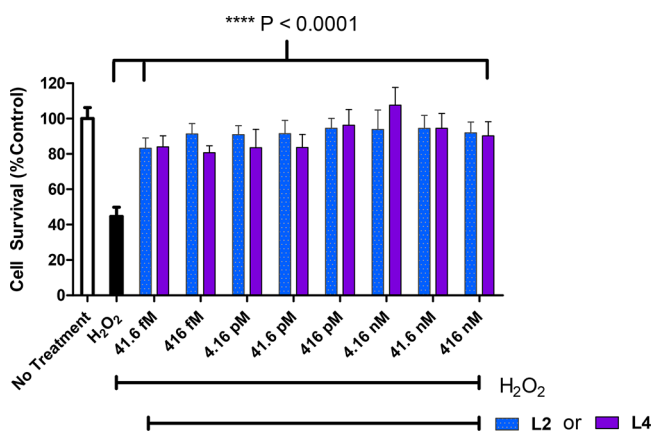


**Figure 9.** MTT cell survival assay of BV2 MGCs after exposure to L2 or L4 at concentrations of 0.0  $\mu$ M to 750 nM and 0.533 mM H<sub>2</sub>O<sub>2</sub> for 16 h. The final concentrations are shown. (\*\*\*\*) Significance with respect to the H<sub>2</sub>O<sub>2</sub> control ( $n = 8$ ) and  $P < 0.0001$  ( $n = 8$ ).

similar to the response observed in HT-22 cells described above. However, the cell viability was recovered (80–100%) with femtomolar-to-nanomolar concentrations of both molecules evaluated; no statistical differences between the L2 and L4 data sets were observed, suggesting that both are effective at preventing cell death from oxidative stress at very small concentrations in the MGC model.

**Metabolic Stability.** The metabolic stability is a major consideration when screening new drug entities for favorable pharmacokinetic properties.<sup>104</sup> It is a measurable parameter that refers to the susceptibility of compounds to biotransformation. Both oral bioavailability and the plasma half-life of a compound are closely tied to the metabolic stability of a molecule. These factors impact the efficacy of the drug. Therefore, L4 was evaluated using two in vitro assay approaches to gauge applicability as a therapeutic.

The oxidation or reduction reactions facilitated by cytochrome P450 and flavin monooxygenase enzymes are described as phase I metabolism and can be modeled using liver microsomes in the presence of an nicotinamide adenine dinucleotide phosphate (NADPH)-regenerating system.<sup>105–107</sup>

In addition, intact hepatocytes are a model commonly used in drug discovery and preclinical drug development to establish the impact of drug-metabolizing enzymes related to four categories of xenobiotic biotransformation: hydrolysis, reduction, oxidation, and conjugation, which encompass both phase I and II metabolism.<sup>108</sup> The method of substrate depletion was used to determine the in vitro half-life.<sup>109</sup> As illustrated in Figure S9, molecule L4 exhibited high stability in microsomes with a half-life greater than 120 min and 77% of molecule L4 was retained at the termination of the experiment. From this data, L4 is classified as a low-intermediate clearance molecule based on the intrinsic clearance ( $Cl_{int}$ ) value of 5.40  $\mu$ L/min/mg.<sup>110</sup> Likewise, exceptional stability was observed with only

31% of L4 depleted over the time course of the experiment in hepatocytes. The half-life for molecule L4 (>240 min) and calculated  $Cl_{int} = 0.20 \mu$ L/min/million cells are consistent with low clearance. The strong  $T_{1/2}$  and  $Cl_{int}$  values in both models suggest that L4 will have slow clearance, thus increasing the potential for delivery of the molecule to the blood–brain barrier.

**Cost Analysis.** Finally, the cost of production is a consistent concern among researchers in academia and industry. Several high-profile news stories have highlighted the exorbitant cost of pharmaceuticals.<sup>111,112</sup> Therefore, we carried out a Cost of Academic Methodology (CAM) analysis for the synthesis of L4 as a means of understanding the potential impact of production costs.<sup>113</sup> In this analysis, the CAM (\$/mol) is equal to the sum of all prices (\$/mol) for the reagents and catalysts divided by the reaction yield. The analysis does not include the cost of standard reagents (NaOH or HCl, for example), workup, or labor, but this approach gives a general sense of the overall comparative cost. The CAM for L4 (\$2926.81/mol) is 85% less than that of L2 thanks to the lack of expensive catalysts required for the removal of protecting groups (Figure S11). This analysis converts to an estimated cost of \$7.67 for each gram of L4 produced, which would classify this as an inexpensive molecule.<sup>113</sup>

## CONCLUSIONS

With the need for new molecules to be tested as therapeutics for neurodegenerative diseases derived from oxidative stress, a new bispyridol containing a tetraaza macrocycle was produced. The success of the design of the water-soluble, new molecule (L4) was evaluated by testing the antioxidant activity through a series of assays and other studies. Radical quenching was established using DPPH<sup>•</sup> assay, while halting the redox cycling of copper(II) in the presence of oxygen and ascorbate was evaluated using CCA assay. In both studies, L4 was shown to outperform the parent pyridinophane L2. As suggested by CCA assay, L4 binds copper(II) in a tetradentate fashion that stabilizes the copper(II) species based on XRD and CV studies. Furthermore, potentiometric data established that L4 has an ideal pI value of 7.3 for pharmaceuticals. The toxicity and metabolic stability data in cellular models show remarkable resistance to metabolism and low toxicity, thus further encouraging more studies of L4 as a potential pharmacological target to treat disorders associated with oxidative stress. Cell studies in neuronal (HT-22) and MGC (BV2) cultures indicate that L4, in particular, is a potent antioxidant and inexpensive molecule that is capable of activating the Nrf2 pathway as an addition mechanism for protection against oxidative stress. Altogether, this work shows how a simple molecule can be designed using fundamental chemical principles based on reactivity and coordination chemistry to produce a highly functional potential therapeutic system that will be explored in more biological contexts in future work.

## EXPERIMENTAL METHODS

**Caution!** Perchlorate salts are explosive and should be handled with care; such compounds should never be heated as solids. All chemical reagents were purchased from either Millipore Sigma or Alfa Aesar and used without further purification. Molecules L1–L3 and 1 were produced using previously reported methods.<sup>67,78,99,114,115</sup> The 12-membered tetraaza macrocycles L1–L4 were isolated as hydrochloride salts prior to metal-ion complexation, in accordance with standard practices.

Elemental analyses were performed by Canadian Microanalytical Services Ltd.

**Physical Measurements.** Electrospray ionization mass spectrometry (ESI-MS) spectral analysis was performed on an Agilent 1200 series 6224 time-of-flight liquid chromatography/mass spectrometry (LC-MS) spectrometer at 175 V (positive ESI scan) in water, MeOH, CHCl<sub>3</sub>, or CH<sub>2</sub>Cl<sub>2</sub>. <sup>1</sup>H and <sup>13</sup>C NMR spectroscopies were carried out in deuterated solvents at 25 °C. All spectra reported were obtained on a Bruker Avance III (400 MHz) high-performance digital NMR spectrometer. Electronic absorption spectra were collected between 190 and 1100 nm using an Agilent 8453 UV-vis spectrophotometer and a 3 mL quartz cuvette with a path length of 1.0 cm. Molar extinction coefficients were calculated utilizing the Beer-Lambert law ( $A = \epsilon bc$ ).

**Synthesis of Tosylamide Monosodium Salt (TsNHNa).** TsNHNa was prepared according to literature procedures.<sup>62,64</sup> Under reflux conditions, solid *p*-toluenesulfonamide (60.0 g, 0.35 mol) was added to sodium ethoxide (23.8 g, 0.35 mol) in absolute ethanol (400 mL). This mixture was stirred under reflux conditions for 2 h and then cooled. The insoluble TsNHNa salt was collected via vacuum filtration and subsequently washed with absolute ethanol. The isolated white solid (TsNHNa) was dried in vacuo to give >90% yield. TsNHNa was used without further purification and can be stored indefinitely.

**Synthesis of Protected 8,17-Benzoyloxy-4,13-bis(*p*-toluenesulfonyl)-1,4,11,13-tetraazabis(2,6-pyridinophane) (2).** TsNHNa (1.93 g, 10 mmol) was dissolved in 200 mL of DMF, placed under N<sub>2</sub>, and heated to 80 °C. **1** (2.82 g, 10 mmol) was dissolved in 50 mL of DMF and added dropwise to the above solution via an addition funnel. Upon complete addition of TsNHNa, the reaction mixture was stirred for 1 h. Next, a second 1 equiv of TsNHNa (1.93 g, 10 mmol) was added (as a solid) to the reaction all at once. The reaction was stirred for an additional 12 h at 80 °C under N<sub>2</sub>. Upon reaction completion, the solvent was evaporated under reduced pressure. Toluene was added to help form an azeotrope. When about 5 mL of the solvent remained, an excess of cold MeOH was added; **2** precipitated as an off-white powder. This mixture was placed in a refrigerator for 12 h. Afterward, the mixture was vacuum-filtered and the collected solid was washed with cold MeOH. **2** was isolated as an off-white powder (3.11 g, 4 mmol, 40% yield).<sup>62-64</sup> Crystals suitable for X-ray analysis were obtained via solvent diffusion of DMF and MeOH.

**Synthesis of 1,4,11,13-Tetraazabis(2,6-pyridinophane)-8,17-diol (L4).** Lithium metal (1.3 g, 187 mmol) was cautiously weighed out and cut into small pieces to expose unoxidized lithium metal. These small pieces of lithium were added to a flask with 150 mL of dry tetrahydrofuran (THF). Naphthalene (3.0 g, 23 mmol) was weighed out and added all at once to the flask. To produce the lithium naphthalenide radical, the solution was stirred and then sonicated until a dark-green color developed, indicating formation of the radical species. The resulting dark-green solution was cooled to -78 °C in a dry ice/acetone bath. **2** (2.6 g, 3.4 mmol) was dissolved in 100 mL of THF to form a brown slurry. This slurry was added dropwise to the lithium naphthalenide solution in the flask. After complete addition of **2**, the reaction mixture was allowed to slowly warm to room temperature. The reaction was then stirred at room temperature for 12 h. Afterward, the reaction mixture was placed on ice and hydrolyzed with water, a precipitate developed, and the solution had a light-brown color. Upon quenching with water, 6 M HCl and then 1 M HCl was added to the reaction until there was no longer a discernible layer between the water and THF, and no additional color change was observed. This aqueous solution was washed several times with diethyl ether. After extraction with diethyl ether, the aqueous layer was evaporated under reduced pressure until about 15 mL of solution was present. The remaining yellow solution was transferred to a falcon tube and evaporated using a lyophilizer. The resulting semidry solid was dissolved in a minimal amount of MeOH. To this solution were added copious amounts of ether and additional MeOH until an off-white solid precipitated. This mixture was left to stir for several hours. The solution was vacuum-filtered, and the collected

solid was washed with diethyl ether. **L4** was isolated as an off-white solid. Yield: 0.502 g (54%). <sup>1</sup>H NMR (400 MHz, D<sub>2</sub>O, 25 °C):  $\delta$  6.54 (s, 4H), 4.38 (s, 8H). <sup>13</sup>C NMR (101 MHz, D<sub>2</sub>O, 25 °C):  $\delta$  165.5, 151.3, 111.7, 52.1.<sup>66</sup> Electronic absorption [H<sub>2</sub>O;  $\lambda_{\text{max}}$  nm ( $\epsilon$ , M<sup>-1</sup> cm<sup>-1</sup>): 255 (4400, sh). Elem anal. Found (calcd) for L4·3HCl·H<sub>2</sub>O·0.5CH<sub>3</sub>OH: C, 41.51 (41.51); H, 5.64 (5.64); N, 12.38 (12.38).

**Equilibrium Measurements.** The reagents used in these studies were of the highest analytical grade obtained from companies such as Millipore, Sigma, Alfa Aesar, or Strem Chemicals Inc.

The pH-potentiometric titrations were carried out with a Metrohm 888 Titrand workstation, using a Metrohm 6.0234.100 combined electrode. The titrated solutions (6.00 mL) were thermostated at 25 °C, the samples were stirred, and N<sub>2</sub> was bubbled through the solution to avoid the effect of CO<sub>2</sub>. Calibration of the electrode was performed using a two-point calibration with potassium hydrogen phthalate (pH = 4.008) and borax (pH = 9.177) buffers.

The concentration of **L4** was determined by pH-potentiometric titration. In the pH-potentiometric titrations, 200–360 mL pH data pairs were recorded in the pH range of 1.6–12.0. Calculation of [H<sup>+</sup>] from the measured pH values was performed with use of the method proposed by Irving and Miles<sup>116</sup> by titrating a 0.02 M HCl solution ( $I = 0.15$  M NaCl) with a standardized NaOH solution (0.2 M). The differences between the measured (pH<sub>read</sub>) and calculated pH ( $-\log [H^+]$ ) values were used to obtain the equilibrium H<sup>+</sup> concentrations from the pH data obtained in the titrations. The ion product of water was determined from the same experiment in the pH range of 11.8–12.0. The protonation constants were calculated from the titration data with the PSEQUAD program.<sup>117</sup>

For the <sup>1</sup>H NMR titrations, the adjustment of pD was carried out with a Mettler Toledo SevenCompact pH/Ion S220 instrument equipped with a Mettler Toledo InLab NMR pH electrode.  $-\log [H^+]$  was measured directly in the NMR tube, after calibration of the electrode with buffered aqueous solutions (pH 4.00, 7.00, and 10.00), and the final pD was calculated by the equation  $pD = pH + 0.40$ .<sup>118</sup> A solution of **L4** ( $c \approx 0.02$  M) was made in D<sub>2</sub>O, and the pD was adjusted by adding 20% DCl in D<sub>2</sub>O or CO<sub>2</sub>-free 40% NaOD in D<sub>2</sub>O. Sodium 2,2-dimethyl-2-silapentane-5-sulfonate was used as an internal reference. UV absorption spectra for the spectrophotometric titrations were collected between 200 and 400 nm using an Agilent Cary 60 UV-vis spectrophotometer and semimicro quartz cuvettes with a path length of 1.0 cm. The pH of the **L4** solution ( $c = 0.02$  M) was adjusted using solid NaOH and HCl gas.

**Preparation of [Cu(L4)Cl]<sub>2</sub>Cl<sub>2</sub> (CuL4).** Molecule **L4** (42.5 mg, 0.123 mmol) was weighed out and dissolved in 5 mL of water to give a clear-light yellow solution. The pH of the ligand solution was adjusted to 5.5 using a 1.0 M solution of KOH. Cu(ClO<sub>4</sub>)<sub>2</sub>·6H<sub>2</sub>O (45.6 mg, 0.123 mmol) was subsequently weighed out and dissolved in 1 mL of water. The metal solution was slowly added dropwise to the pH-adjusted ligand solution to initiate metalation. Immediately the solution color changed from light yellow to light blue; this solution was stirred at room temperature, open to air, for 24 h. The reaction mixture was subsequently evaporated under reduced pressure to afford a light-green solid. The solid was dissolved in a minimum amount of MeOH (1 mL), and a very small amount of water was added (0.8 mL). Any remaining salts left undissolved were filtered out of the solution; the filtered solution was set out for crystal growth. After several days, more salts precipitated; these were subsequently removed by filtration, and the solutions were set out for slow evaporation and crystallization again. After several cycles of filtering the solution and setting it out for slow evaporation, light-green X-ray-quality crystals of **CuL4** were isolated (15.1 mg, 0.017 mmol, 28% yield). Electronic absorption [H<sub>2</sub>O;  $\lambda_{\text{max}}$  nm ( $\epsilon$ , M<sup>-1</sup> cm<sup>-1</sup>): 758 (23). Electronic absorption [DMF;  $\lambda_{\text{max}}$  nm ( $\epsilon$ , M<sup>-1</sup> cm<sup>-1</sup>): 873 (49). ESI-MS<sup>+</sup>. Calcd for [CuL4Cl]<sup>+</sup> = [M]<sup>+</sup> (Found):  $m/z$  370.0258 (369.8742).

**X-ray Crystallography.** A Leica MZ 75 microscope was used to identify samples suitable for analysis. A Bruker APEX-II CCD diffractometer was employed for crystal screening, unit cell determination, and data collection, which was obtained at 100 K. The Bruker D8 goniometer was controlled using the APEX3 software

suite, version 1.<sup>119</sup> The samples were optically centered with the aid of a video camera, so that no translations were observed as the crystal was rotated through all positions. The X-ray radiation employed was generated from a Mo  $K\alpha$  sealed X-ray tube ( $\lambda = 0.71076$ ) with a potential of 50 kV and a current of 30 mA and fitted with a graphite monochromator in the parallel mode (175 mm collimator with 0.5 mm pinholes).

**CuL4 (CCDC 1910897) Structure Determination.** A translucent light-green blocklike crystal of CuL4 ( $0.279 \times 0.160 \times 0.126$  mm) was mounted on a 150  $\mu\text{m}$  cryoloop and used for X-ray crystallographic analysis. The crystal-to-detector distance was set to 50 mm, and the exposure time was 10 s/deg for all data sets at a scan width of  $0.5^\circ$ . A total of 2180 frames were collected, and the data collection was 99% complete. The frames were integrated with the Bruker SAINT software package<sup>120</sup> using a narrow-frame algorithm. Integration of the data used a monoclinic unit cell, yielding a total of 45954 reflections to a maximum  $\theta$  angle of  $30.13^\circ$  ( $0.71 \text{ \AA}$  resolution), of which 5217 reflections were independent with  $R_{\text{int}} = 4.99\%$ . The data were corrected for absorption effects using the multiscan method SADABS.<sup>121</sup> Using Olex2,<sup>122</sup> the structure was solved with the SHELXS<sup>123</sup> structure solution program using direct methods and refined with the SHELXL<sup>124</sup> refinement package using least-squares minimization. All H and non-H atoms were refined using anisotropic thermal parameters. The thermal ellipsoid molecular plots (50%) were produced using Olex2.<sup>122</sup>

**Electrochemical Measurements.** CV was carried out with an EC Epsilon potentiostat (C-3 cell stand) purchased from BASi Analytical Instruments (West Lafayette, IN). A glassy carbon (GC) electrode from BASi (MF-2012), 3 mm in diameter, was polished on a white nylon pad (BASi MF-2058) with different-sized diamond polishes (15, 6, and 1  $\mu\text{m}$ ) to ensure a mirrorlike finish. Between each measurement, the GC electrode was polished with three diamond polishes. A three-electrode cell configuration was used with GC as the working electrode, a silver wire (0.5 mm diameter) quasi-reference electrode housed in a glass tube (7.5 cm  $\times$  5.7 mm) with a porous CoralPor tip, and a platinum wire (7.5 cm) as the counter electrode (BASi MW-1032). All solutions were bubbled with  $\text{N}_2$  gas for at least 15 min prior to experimentation and kept under a humidified  $\text{N}_2$  gas blanket. All potentials herein are reported versus  $\text{Fc}/\text{Fc}^+$  ( $E_{1/2} = 0.0$  V). For each electrochemical analysis, 3.0 mg of complex was dissolved in 3.0 mL of anhydrous DMF containing 0.1 M tetrabutylammonium perchlorate as the supporting electrolyte.

**DPPH<sup>•</sup> Assay.** A stock solution of DPPH<sup>•</sup> was prepared by dissolving 17.8 mg in 300 mL of MeOH (150  $\mu\text{M}$ ). A solid sample of L4 or BHT was dissolved in 10 mL of MeOH (stock concentration 5 mM). A solid sample of L2 was dissolved in 10 mL of water, and the pH was adjusted to 7 using 1.0 M KOH. The water was then removed, and the sample was dissolved in 10 mL of MeOH (stock concentration 5 mM). Next, the sample solutions were prepared in 7 mL vials by diluting the stock solutions (5 mM) with MeOH to various concentrations (2–3000  $\mu\text{M}$ , 1 mL). Next, each working sample was prepared by mixing 100  $\mu\text{L}$  of one of the prepared samples with 100  $\mu\text{L}$  of the DPPH stock directly in the 96-well plate to a final concentration ranging from 1 to 1500  $\mu\text{M}$ . A separate well plate was used for each sample, and each concentration was analyzed in triplicate. An aliquot of the DPPH stock solution (100  $\mu\text{L}$ ) was mixed with MeOH (100  $\mu\text{L}$ ) and used as a negative control for each sample. The samples were incubated in the dark for 30 min at room temperature. For analysis, each well plate was run using the BMG Labtech FLUOstar Omega UV/vis absorbance spectrophotometer microplate reader, and the absorbance at 516 nm of each sample was measured. Each experiment was performed in triplicate ( $n = 3$ ). The final absorbance values have been normalized to the average ( $n = 3$ ) absorbance of the negative control DPPH sample and are expressed as the percentage of DPPH<sup>•</sup> quenched.

**CCA Assay.** All solutions were prepared in a phosphate-buffered saline (PBS) buffer (1X, pH 7.4) except  $\text{CuSO}_4 \cdot 6\text{H}_2\text{O}$ , which was dissolved and diluted in Milli-Q water. The final sample volume was 3 mL. Each experiment was performed in triplicate ( $n = 3$ ). Hydroxyl radical production was followed by measuring the conversion of CCA

into 7-hydroxy-CCA ( $\lambda_{\text{ex}} = 395$  nm and  $\lambda_{\text{em}} = 450$  nm). The general order of addition is as follows: PBS buffer (2200  $\mu\text{L}$  for positive control, 2150  $\mu\text{L}$  for 0.5 equiv samples, 2100  $\mu\text{L}$  for 1 equiv samples, and 2300  $\mu\text{L}$  for negative controls), CCA (100  $\mu\text{M}$ , 500  $\mu\text{L}$ ), Desferal (1  $\mu\text{M}$ , 100  $\mu\text{L}$ ),<sup>95,125</sup> molecule L2 or L4 ( $1/2$  equiv = 5  $\mu\text{M}$ , 50  $\mu\text{L}$ ; 1 equiv = 10  $\mu\text{M}$ , 100  $\mu\text{L}$ ), copper(II) (10  $\mu\text{M}$ , 100  $\mu\text{L}$ ), and then ascorbate (300  $\mu\text{M}$ , 100  $\mu\text{L}$ ).

**Cell Culture Methods.** HT-22 Cell Culture. The mouse neuronal hippocampal cell line (HT-22) were obtained from the UNT Health Science Center. HT-22 cells were cultured in Dulbecco's modified Eagle's medium (DMEM), supplemented with 100 units/mL penicillin/100  $\mu\text{g}/\text{mL}$ , streptomycin, 1 mM L-glutamine (100 mM, 5 mL), and charcoal-stripped fetal bovine serum (FBS; 15%, Sigma-Aldrich). Both cell lines were grown in a water-jacketed incubator at  $37^\circ\text{C}$  with 5%  $\text{CO}_2$  and 95% air atmospheric conditions. To prepare dilutions of compounds, the same media were used excluding the addition of the serum and antibiotics.

**Cell Viability in HT-22.** 3-(4,5-Dimethylthiazolyl-2)-2,5-diphenyltetrazolium bromide (MTT) assay was used to determine the cell-line sensitivity to the drugs used in this study. To perform this assay,  $5 \times 10^3$  cells/well were plated into 96-well plates for 24 h and then treated with increasing concentrations of the molecule of interest in replicates of 8 and incubated for 16 h at  $37^\circ\text{C}$ . The medium was replaced by 100  $\mu\text{L}$  of 1 mg/mL MTT in a serum-free medium. The cells were then incubated for 4 h at  $37^\circ\text{C}$ , after which MTT was replaced by 100  $\mu\text{L}$  of dimethyl sulfoxide (DMSO) to solubilize the precipitate. The plate was placed in a shaker for 5 min, and the absorbance was measured at 540 nm using a plate reader (Molecular Dynamics). The data obtained were processed using GraphPad Prism 5 for Windows to determine the  $\text{EC}_{50}$  values presented. Analysis tables are available in the Supporting Information.

**Cell Viability Assay for  $\text{H}_2\text{O}_2$  Studies.** The cell viability was measured by a colorimetric cell viability kit (PK-CA705-CK04; Promokine, Heidelberg, Germany) with the tetrazolium salt WST-8 [2-(2-methoxy-4-nitrophenyl)-3-(4-nitrophenyl)-5-(2,4-disulfophenyl)-2H-tetrazolium, monosodium salt], which can be bioreduced to a water-soluble orange formazan dye by dehydrogenases present in the viable cells. The amount of formazan produced is directly proportional to the number of living cells. Cells were incubated with or without L2 and L4 for 24 h and then treated with 600  $\mu\text{M}$   $\text{H}_2\text{O}_2$  for 4 h. After treatment, 10  $\mu\text{L}$  of the WST-8 solution was added to each well of the culture plate and incubated for 2 h in the incubator. The absorption was evaluated at 450 nm using a microplate reader (BioTek, Winooski, VT).

**Western Blot Analysis.** The protein concentration was determined with a BCA assay kit (23225; Thermo Scientific, Rockford, IL). Equal amounts of protein were boiled in a Laemmli buffer (Bio-Rad, Richmond, CA), loaded onto 12% sodium dodecyl sulfate polyacrylamide gel electrophoresis gel, and transferred to a 0.2  $\mu\text{m}$  poly(vinylidene difluoride) membrane (GE Healthcare, Boulder, CO). The membranes were incubated with the appropriate primary antibodies overnight at  $4^\circ\text{C}$  and then incubated with the appropriate secondary antibodies for 1 h. Detection was performed using an ECL Western blotting detection system (Thermo Scientific, Rockford, IL). The immunoblot was analyzed with a Bio-Rad imaging system (Versadoc 5000 MP Imaging System, Bio-Rad, Richmond, CA).

**MGCs.** The BV2 MGCs were a gift from Dr. Meharvan Singh. The BV2 cells were incubated at  $37^\circ\text{C}$  in 5%  $\text{CO}_2$ . Cells were cultured and passaged in 10 cm tissue culture dishes in DMEM, supplemented with 5% L-glutamine, 5% penicillin–streptomycin, and 15% FBS. The BV2 cells were passaged when plates reached 80–90% confluence. A serum-free medium was used for dilutions of compounds.

MTT assay was utilized to measure the cell viability with pretreatment of a L2 or L4 compound, administered 1 h before the induction of oxidative stress. The BV2 cells were first plated in a 96-well plate at a density of 5000 cells/100  $\mu\text{L}$  of the complete medium per well. After 24 h, the antioxidant molecule was added to each well to provide final concentrations of 416 nM to 41.6 fM. Each concentration was replicated in six wells per column, including a control column that did not receive treatment. Following treatment,

the plate was maintained in an incubator for 1 h. To provoke oxidative stress, all cells were then treated with H<sub>2</sub>O<sub>2</sub> at a final concentration of 0.533 mM/well and the plate was then incubated for 16 h. Supernatants were removed, and 100  $\mu$ L of MTT (1 mg/mL serum-free medium) was added to all wells and incubated for 4 h. Subsequently, supernatants were removed, 100  $\mu$ L of DMSO was added to each well, and the plate was placed on a rocker for 5 min. The absorbance was then measured using a plate reader (BMG LabTech FLUOstar Omega) at an absorbance of 540 nm. The data presented were standardized to cells receiving no treatment (100%) and the results of an average of three plates for each compound studied. The data were analyzed with *GraphPad Prism 5* for Windows.

**Mouse Microsome Stability (Phase I).** Male ICR/CD-1 mouse microsomes (Lot ZMC) were purchased from BioIVT (Baltimore, MD). A total 0.25 mg of microsomes was added on ice to a 50 mM Tris, pH 7.5, solution, containing L4 added from a DMSO stock. The final concentration of the compound after the addition of all reagents was 2  $\mu$ M. An NADPH-regenerating system [1.7 mg/mL NADP, 7.8 mg/mL glucose-6-phosphate, 6 U/mL glucose-6-phosphate dehydrogenase in 2% (w/v) NaHCO<sub>3</sub>/10 mM MgCl<sub>2</sub>] was added for analysis of the phase I metabolism. The tube was then placed in a 37 °C shaking water bath. At various time points after the addition of phase I cofactors, the reaction was stopped by the addition of 0.5 mL of MeOH containing an internal standard (IS), tolbutamide, and 0.2% formic acid to quench the reaction and precipitate protein. Time 0 samples were quenched prior to the addition of the compound or NADPH-regenerating system. The samples were incubated 10 min at room temperature and then spun at 16100g for 5 min in a microcentrifuge. The supernatant was analyzed by LC–MS/MS. Analytical methods were developed for each compound using a Sciex 4000 QTRAP (Foster City, CA), a combination triple quadrupole/ion-trap instrument. The parent ion and two most prominent daughter ions were followed to confirm the compound identity, although only the most abundant daughter was used for quantitation. L4 was monitored by the 273.1 to 137.0 transition and the IS tolbutamide by the 269.1 to 169.9 transition using the following ion source parameters: CUR = 25, CAD = high, IS = 4000, TEM = 600, GS1 = 70, and GS2 = 70. A Shimadzu Prominence liquid chromatograph (Columbia, MD) with a Phenomenex Luna C8 (5  $\mu$ m packing; 100  $\times$  4.6 mm; Torrance, CA) was used for chromatography under the following conditions: buffer A, water + 0.1% formic acid; buffer B, MeOH + 0.1% formic acid; flow rate, 0.7 mL/min; 0–2 min gradient to 1% B, 2.0–3.0 min gradient to 95% B, 3.0–4.0 min gradient to 95% B, and 4.0–4.1 min gradient to 1% B and 4.1–5.0 1% B.

**Mouse Hepatocyte Stability (Phases I and II).** L4 (DMSO stock, 2  $\mu$ M final concentration) was incubated with murine hepatocytes (Lot NNS) for 0–240 min at 37 °C and 5% CO<sub>2</sub>. The final concentration of hepatocytes in the reaction was 1  $\times$  10<sup>6</sup>/mL. The enzymatic reaction was quenched with a 2-fold volume of MeOH containing 0.15% formic acid and the IS tolbutamide. Samples were vortexed for 15 s, incubated at room temperature for 10 min, and spun for 5 min at 16100g. The supernatant was collected and analyzed by LC–MS/MS, as described above for the microsome stability assay.

The method described by McNaney et al.<sup>109</sup> was used with modification for determination of the metabolic stability half-life by substrate depletion. A “% remaining” value was used to assess the metabolic stability of a compound over time. The LC–MS/MS peak area of the incubated sample at each time point was divided by the LC–MS/MS peak area of the time 0 ( $T_0$ ) sample and multiplied by 100. The natural logarithm (ln) of the % remaining of the compound was then plotted versus time (in minutes), and a linear regression curve was plotted going through the  $y$  intercept at ln(100). If the metabolism of a compound failed to show linear kinetics at a later time point, those time points were excluded. The half-life ( $T_{1/2}$ ) was calculated as  $T_{1/2} = 0.693/\text{slope}$ . To determine the intrinsic clearance, the ln peak area ratio (compound peak area/IS peak area) was plotted against time and the gradient of the line determined.<sup>126–129</sup>

## ■ ASSOCIATED CONTENT

### 📄 Supporting Information

The Supporting Information is available free of charge at <https://pubs.acs.org/doi/10.1021/acs.inorgchem.9b02932>.

Reaction schemes, X-ray crystallographic data for **2** and **CuL4**, potentiometric data, and assay data (PDF)

### Accession Codes

CCDC 1910897 contains the supplementary crystallographic data for this paper. These data can be obtained free of charge via [www.ccdc.cam.ac.uk/data\\_request/cif](http://www.ccdc.cam.ac.uk/data_request/cif), or by emailing [data\\_request@ccdc.cam.ac.uk](mailto:data_request@ccdc.cam.ac.uk), or by contacting The Cambridge Crystallographic Data Centre, 12 Union Road, Cambridge CB2 1EZ, UK; fax: +44 1223 336033.

## ■ AUTHOR INFORMATION

### Corresponding Author

\*Email: [kayla.green@tcu.edu](mailto:kayla.green@tcu.edu).

### ORCID

Gyula Tircsó: 0000-0002-7896-7890

Kayla N. Green: 0000-0001-8816-7646

### Author Contributions

The manuscript was written through contributions of all authors. All authors have given approval to the final version of the manuscript.

### Notes

The authors declare no competing financial interest.

## ■ ACKNOWLEDGMENTS

This work was funded by the National Institutes of Health (Grant R15GM123463 to K.N.G., G.A., and M.C.). The authors are also grateful for generous financial support from TCU Andrews Institute of Mathematics & Science Education (to K.N.G.), Cambridge Isotope Laboratories, and a TCU Research and Creativity Activity Grant (to K.N.G.). Metabolic stability studies were conducted by the Preclinical Pharmacology Core at the University of Texas Southwestern Medical Center. Gy.T. is grateful for support from the Hungarian National Research, Development and Innovation Office (Project NKFIH K-120224), and for a János Bolyai Research Scholarship of the Hungarian Academy of Sciences. Gy.T. thankful for a scholarship supported by the ÚNKP-18-4 New National Excellence Program of the Ministry of Human Capacities. The research was also supported, in part, by the European Union and cofinanced by the European Regional Development Fund under Projects GINOP-2.3.2-15-2016-00008 and GINOP-2.3.3-15-2016-00004 to Gy.T. The Table of Contents background picture is by Jason Sells of College Station, TX, and was used with his permission.

## ■ REFERENCES

- (1) Alzheimer's Disease Facts and Figures. *Alzheimer's & Dementia*; Alzheimer's Association, 2016; Vol. 12, Part 4.
- (2) Spotlight on Neurodegenerative diseases: dementia 2016 (accessed February 29, 2016).
- (3) Doig, A. J.; Del Castillo-Frias, M. P.; Berthoumieu, O.; Tarus, B.; Nasica-Labouze, J.; Sterpone, F.; Nguyen, P. H.; Hooper, N. M.; Faller, P.; Derreumaux, P. Why Is Research on Amyloid-beta Failing to Give New Drugs for Alzheimer's Disease? *ACS Chem. Neurosci.* **2017**, *8* (7), 1435–1437.
- (4) Santilli, F.; D'Ardes, D.; Davi, G. Oxidative stress in chronic vascular disease: From prediction to prevention. *Vasc. Pharmacol.* **2015**, *74*, 23–37.

- (5) Czernska, M.; Mikolajewska, K.; Zielinski, M.; Gromadzinska, J.; Wasowicz, W. Today's oxidative stress markers. *Med. Pr.* **2015**, *66* (3), 393.
- (6) Gandhi, S.; Abramov, A. Y. Mechanism of oxidative stress in neurodegeneration. *Oxid. Med. Cell. Longevity* **2012**, *2012*, 428010.
- (7) Dasuri, K.; Zhang, L.; Keller, J. N. Oxidative stress, neurodegeneration, and the balance of protein degradation and protein synthesis. *Free Radical Biol. Med.* **2013**, *62*, 170–185.
- (8) Federico, A.; Cardaioli, E.; Da Pozzo, P.; Formichi, P.; Gallus, G. N.; Radi, E. Mitochondria, oxidative stress and neurodegeneration. *J. Neurol. Sci.* **2012**, *322* (1–2), 254–262.
- (9) Tramutola, A.; Lanzillotta, C.; Perluigi, M.; Butterfield, D. A. Oxidative stress, protein modification and Alzheimer disease. *Brain Res. Bull.* **2017**, *133*, 88–96.
- (10) Savelieff, M. G.; Lee, S.; Liu, Y.; Lim, M. H. Untangling Amyloid- $\beta$ , Tau, and Metals in Alzheimer's Disease. *ACS Chem. Biol.* **2013**, *8* (5), 856–865.
- (11) Bonda, D. J.; Lee, H.-g.; Blair, J. A.; Zhu, X.; Perry, G.; Smith, M. A. Role of metal dyshomeostasis in Alzheimer's disease. *Metallomics* **2011**, *3* (3), 267–270.
- (12) Kepp, K. P. Bioinorganic Chemistry of Alzheimer's Disease. *Chem. Rev.* **2012**, *112* (10), 5193–5239.
- (13) Savelieff, M. G.; DeToma, A. S.; Derrick, J. S.; Lim, M. H. The ongoing search for small molecules to study metal-associated amyloid-beta species in Alzheimer's disease. *Acc. Chem. Res.* **2014**, *47* (8), 2475–82.
- (14) Jakob-Roetne, R.; Jacobsen, H. Alzheimer's disease: from pathology to therapeutic approaches. *Angew. Chem., Int. Ed.* **2009**, *48*, 3030–3059.
- (15) Kalia, L. V.; Lang, A. E. Parkinson's disease. *Lancet* **2015**, *386* (9996), 896–912.
- (16) Brown, R. H.; Al-Chalabi, A. Amyotrophic lateral sclerosis. *N. Engl. J. Med.* **2017**, *377* (2), 162–172.
- (17) Al-Chalabi, A.; Hardiman, O. The epidemiology of ALS: a conspiracy of genes, environment and time. *Nat. Rev. Neurol.* **2013**, *9* (11), 617.
- (18) Hunsaker, E. W.; Franz, K. J. Emerging Opportunities To Manipulate Metal Trafficking for Therapeutic Benefit. *Inorg. Chem.* **2019**, *58*, 13528.
- (19) Guilloreau, L.; Combalbert, S.; Sournia-Saquet, A.; Mazarguil, H.; Faller, P. Redox Chemistry of Copper–Amyloid- $\beta$ : The Generation of Hydroxyl Radical in the Presence of Ascorbate is Linked to Redox-Potentials and Aggregation State. *ChemBioChem* **2007**, *8* (11), 1317–1325.
- (20) Duce, J. A.; Bush, A. I. Biological metals and Alzheimer's disease: Implications for therapeutics and diagnostics. *Prog. Neurobiol. (Oxford, U. K.)* **2010**, *92* (1), 1–18.
- (21) Que, E. L.; Domaille, D. W.; Chang, C. J. Metals in Neurobiology: Probing Their Chemistry and Biology with Molecular Imaging. *Chem. Rev.* **2008**, *108*, 1517–1549.
- (22) Hureau, C.; Faller, P. Abeta-mediated ROS production by Cu ions: structural insights, mechanisms and relevance to Alzheimer's disease. *Biochimie* **2009**, *91* (10), 1212–7.
- (23) Savelieff, M. G.; Nam, G.; Kang, J.; Lee, H. J.; Lee, M.; Lim, M. H. Development of Multifunctional Molecules as Potential Therapeutic Candidates for Alzheimer's Disease, Parkinson's Disease, and Amyotrophic Lateral Sclerosis in the Last Decade. *Chem. Rev.* **2019**, *119* (2), 1221–1322.
- (24) Boros, E.; Rybak-Akimova, E.; Holland, J. P.; Rietz, T.; Rotile, N.; Blasi, F.; Day, H.; Latifi, R.; Caravan, P. Pycup-A Bifunctional, Cage-like Ligand for Cu-64 Radiolabeling. *Mol. Pharmaceutics* **2014**, *11* (2), 617–629.
- (25) Chow, T. W.-S.; Wong, E. L.-M.; Guo, Z.; Liu, Y.; Huang, J.-S.; Che, C.-M. Cis-dihydroxylation of alkenes with oxone catalyzed by iron complexes of a macrocyclic tetraaza ligand and reaction mechanism by ESI-MS spectrometry and DFT calculations. *J. Am. Chem. Soc.* **2010**, *132* (38), 13229–13239.
- (26) Zheng, B.; Tang, F.; Luo, J.; Schultz, J. W.; Rath, N. P.; Mirica, L. M. Organometallic nickel (III) complexes relevant to cross-coupling and carbon–heteroatom bond formation reactions. *J. Am. Chem. Soc.* **2014**, *136* (17), 6499–6504.
- (27) Cho, J.; Sarangi, R.; Annaraj, J.; Kim, S. Y.; Kubo, M.; Ogura, T.; Solomon, E. I.; Nam, W. Geometric and electronic structure and reactivity of a mononuclear 'side-on'nickel (III)–peroxo complex. *Nat. Chem.* **2009**, *1* (7), 568.
- (28) Krüger, H.-J. Spin transition in octahedral metal complexes containing tetraazamacrocyclic ligands. *Coord. Chem. Rev.* **2009**, *253* (19–20), 2450–2459.
- (29) Koch, W. O.; Krüger, H. J. A Highly Reactive and Catalytically Active Model System for Intradiol-Cleaving Catechol Dioxygenases: Structure and Reactivity of Iron (III) Catecholate Complexes of N, N'-Dimethyl-2,11-diaza[3.3](2,6)pyridinophane. *Angew. Chem., Int. Ed. Engl.* **1996**, *34* (23–24), 2671–2674.
- (30) Koch, W. O.; Krüger, H.-J. A Highly Reactive and Catalytically Active Model System for Intradiol-Cleaving Catechol Dioxygenases: Structure and Reactivity of Iron(III) Catecholate Complexes of N, N'-Dimethyl-2,11-diaza[3.3](2,6)pyridinophane. *Angew. Chem., Int. Ed. Engl.* **1996**, *34* (23–24), 2671–2674.
- (31) Koch, W. O.; Barbieri, A.; Grodzicki, M.; Schunemann, V.; Trautwein, A. X.; Krüger, H. J. Eight-coordinate iron(II) and iron(III) ions in complexes with distorted dodecahedral FeN8 environments: Synthesis and structures of bis(2,11-diaza[3.3](2,6)pyridinophane)-iron complexes. *Angew. Chem., Int. Ed. Engl.* **1996**, *35* (4), 422–424.
- (32) Xu, S.; Bucinsky, L.; Breza, M.; Krzystek, J.; Chen, C. H.; Pink, M.; Telsler, J.; Smith, J. M. Ligand Substituent Effects in Manganese Pyridinophane Complexes: Implications for Oxygen-Evolving Catalysis. *Inorg. Chem.* **2017**, *56* (22), 14315–14325.
- (33) Lee, W. T.; Munoz, S. B., 3rd; Dickie, D. A.; Smith, J. M. Ligand modification transforms a catalase mimic into a water oxidation catalyst. *Angew. Chem., Int. Ed.* **2014**, *53* (37), 9856–9.
- (34) Tseberlidis, G.; Intrieri, D.; Caselli, A. Catalytic Applications of Pyridine-Containing Macrocyclic Complexes. *Eur. J. Inorg. Chem.* **2017**, *2017* (30), 3589–3603.
- (35) Wessel, A. J.; Schultz, J. W.; Tang, F.; Duan, H.; Mirica, L. M. Improved synthesis of symmetrically & asymmetrically N-substituted pyridinophane derivatives. *Org. Biomol. Chem.* **2017**, *15* (46), 9923–9931.
- (36) Shkil, G. P.; Sagitullin, R. S. Pyridinophanes (a review). *Chem. Heterocycl. Compd.* **1998**, *34* (5), 507.
- (37) Koch, W. O.; Schünemann, V.; Gerdan, M.; Trautwein, A. X.; Krüger, H. Evidence for an unusual thermally induced low-spin ( $S = 1/2$ ) reversible arrow intermediate-spin ( $S = 3/2$ ) transition in a six-coordinate iron(III) complex: Structure and electronic properties of a (1,2-benzenedithiolato)iron(III) complex containing N, N'-dimethyl-2,11-diaza[3.3](2,6)pyridinophane as ligand. *Chem. - Eur. J.* **1998**, *4*, 686–691.
- (38) Gamba, I.; Codolà, Z.; Lloret-Fillol, J.; Costas, M. Making and breaking of the OO bond at iron complexes. *Coord. Chem. Rev.* **2017**, *334*, 2–24.
- (39) Serrano-Plana, J.; Aguinaco, A.; Belda, R.; García-España, E.; Basallote, M. G.; Company, A.; Costas, M. Exceedingly Fast Oxygen Atom Transfer to Olefins via a Catalytically Competent Nonheme Iron Species. *Angew. Chem., Int. Ed.* **2016**, *55* (21), 6310–6314.
- (40) Raffard, N.; Carina, R.; Simaan, A. J.; Sinton, J.; Riviere, E.; Tchertanov, L.; Bourcier, S.; Bouchoux, G.; Delroisse, M.; Banse, F.; Girerd, J. J. Biomimetic catalysis of catechol cleavage by O-2 in organic solvents - Role of accessibility of O-2 to Fe-III in 2,11-diaza[3.3](2,6)pyridinophane-type catalysts. *Eur. J. Inorg. Chem.* **2001**, *9*, 2249–2254.
- (41) Lee, W.-T.; Xu, S.; Dickie, D. A.; Smith, J. M. A Robust Mn Catalyst for H<sub>2</sub>O<sub>2</sub> Disproportionation in Aqueous Solution. *Eur. J. Inorg. Chem.* **2013**, *2013* (22–23), 3867–3873.
- (42) Satou, T.; Shinmyozu, T. Synthesis and structural analysis of 2,11-diaza[3.3](3,5)pyridinophane. *J. Chem. Soc. Perk T2* **2002**, No. 3, 393–397.
- (43) Fan, R.; Serrano-Plana, J.; Oloo, W. N.; Draksharapu, A.; Delgado-Pinar, E.; Company, A.; Martin-Diaconescu, V.; Borrell, M.; Lloret-Fillol, J.; Garcia-España, E.; Guo, Y.; Bominaar, E. L.; Que, L.,

- Jr; Costas, M.; Munck, E. Spectroscopic and DFT Characterization of a Highly Reactive Nonheme Fe(V)-Oxo Intermediate. *J. Am. Chem. Soc.* **2018**, *140* (11), 3916–3928.
- (44) Le Fur, M.; Molnár, E.; Beyler, M.; Fougère, O.; Esteban-Gómez, D.; Rousseaux, O.; Tripier, R.; Tircsó, G.; Platas-Iglesias, C. Expanding the Family of PycLen-Based Ligands Bearing Pendant Picolate Arms for Lanthanide Complexation. *Inorg. Chem.* **2018**, *57* (12), 6932–6945.
- (45) Le Fur, M.; Beyler, M.; Lepareur, N.; Fougère, O.; Platas-Iglesias, C.; Rousseaux, O.; Tripier, R. PycLen Tri-*n*-butylphosphonate Ester as Potential Chelator for Targeted Radiotherapy: From Yttrium(III) Complexation to <sup>90</sup>Y Radiolabeling. *Inorg. Chem.* **2016**, *55* (16), 8003–8012.
- (46) Pedrazzini, T.; Pirovano, P.; Dell'Acqua, M.; Ragaini, F.; Illiano, P.; Macchi, P.; Abbiati, G.; Caselli, A. Organometallic Reactivity of [Silver(I)-(Pyridine-Containing Ligand)] Complexes Relevant to Catalysis. *Eur. J. Inorg. Chem.* **2015**, *2015* (30), 5089–5098.
- (47) Rojas-Quijano, F. A.; Tircso, G.; Tircsone Benyo, E.; Baranyai, Z.; Tran Hoang, H.; Kalman, F. K.; Gulaka, P. K.; Kodibagkar, V. D.; Aime, S.; Kovacs, Z.; Sherry, A. D. Synthesis and Characterization of a Hypoxia-Sensitive MRI Probe. *Chem. - Eur. J.* **2012**, *18* (31), 9669–9676.
- (48) Rojas-Quijano, F. A.; Benyo, E. T.; Tircso, G.; Kalman, F. K.; Baranyai, Z.; Aime, S.; Sherry, A. D.; Kovacs, Z. Lanthanide(III) Complexes of Tris(amide) PCTA Derivatives as Potential Bimodal Magnetic Resonance and Optical Imaging Agents. *Chem. - Eur. J.* **2009**, *15* (47), 13188–13200.
- (49) Bedford, R. B.; Brenner, P. B.; Elorriaga, D.; Harvey, J. N.; Nunn, J. The influence of the ligand chelate effect on iron-amine-catalysed Kumada cross-coupling. *Dalton Trans.* **2016**, *45* (40), 15811–15817.
- (50) Lincoln, K. M.; Gonzalez, P.; Richardson, T. E.; Julovich, D. A.; Saunders, R.; Simpkins, J. W.; Green, K. N. A potent antioxidant small molecule aimed at targeting metal-based oxidative stress in neurodegenerative disorders. *Chem. Commun.* **2013**, *49*, 2712–2714.
- (51) Lincoln, K. M.; Richardson, T. E.; Rutter, L.; Gonzalez, P.; Simpkins, J. W.; Green, K. N. An N-heterocyclic amine chelate capable of antioxidant capacity and amyloid disaggregation. *ACS Chem. Neurosci.* **2012**, *3* (11), 919–27.
- (52) Green, K. N.; Pota, K.; Tircsó, G.; Gogolák, R. A.; Kinsinger, O.; Davda, C.; Blain, K.; Brewer, S. M.; Gonzalez, P.; Johnston, H. M.; Akkaraju, G. Dialing in on pharmacological features for a therapeutic antioxidant small molecule. *Dalton Trans.* **2019**, *48*, 12430–12439.
- (53) Lincoln, K. M.; Richardson, T. E.; Rutter, L.; Gonzalez, P.; Simpkins, J. W.; Green, K. N. An N-heterocyclic amine chelate capable of antioxidant capacity and amyloid disaggregation. *ACS Chem. Neurosci.* **2012**, *3* (11), 919–27.
- (54) Xu, J.; Church, S. J.; Patassini, S.; Begley, P.; Waldvogel, H. J.; Curtis, M. A.; Faull, R. L. M.; Unwin, R. D.; Cooper, G. J. S. Evidence for widespread, severe brain copper deficiency in Alzheimer's dementia. *Metallomics* **2017**, *9*, 1106–19.
- (55) Bush, A. I. The metallobiology of Alzheimer's disease. *Trends Neurosci.* **2003**, *26*, 207–14.
- (56) Sastre, M.; Ritchie, C. W.; Hajji, N. Metal ions in Alzheimer's disease brain. *JSM Alzheimer's Dis. Relat. Dement.* **2015**, *2*, 1014.
- (57) Xu, J.; Begley, P.; Church, S. J.; Patassini, S.; McHarg, S.; Kureishy, N.; Hollywood, K. A.; Waldvogel, H. J.; Liu, H.; Zhang, S.; et al. Elevation of brain glucose and polyol-pathway intermediates with accompanying brain-copper deficiency in patients with Alzheimer's disease: metabolic basis for dementia. *Sci. Rep.* **2016**, *6*, 6.
- (58) Bush, A. I. The Metal Theory of Alzheimer's Disease. *J. Alzheimer's Dis.* **2012**, *33*, S277–S281.
- (59) Cardoso, B. R.; Hare, D. J.; Lind, M.; McLean, C. A.; Volitakis, I.; Laws, S. M.; Masters, C. L.; Bush, A. I.; Roberts, B. R. The APOE  $\epsilon$ 4 Allele Is Associated with Lower Selenium Levels in the Brain: Implications for Alzheimer's Disease. *ACS Chem. Neurosci.* **2017**, *8* (7), 1459–1464.
- (60) Xu, J.; Church, S. J.; Patassini, S.; Begley, P.; Waldvogel, H. J.; Curtis, M. A.; Faull, R. L. M.; Unwin, R. D.; Cooper, G. J. S. Evidence for widespread, severe brain copper deficiency in Alzheimer's dementia. *Metallomics* **2017**, *9* (8), 1106–1119.
- (61) Alpha, B.; Anklam, E.; Deschenaux, R.; Lehn, J.-M.; Pietraskiewicz, M. Synthesis and Characterization of the Sodium and Lithium Cryptates of Macrobicyclic Ligands Incorporating Pyridine, Bipyridine, and Biisoquinoline Units. *Helv. Chim. Acta* **1988**, *71*, 1042–1052.
- (62) Bottino, F.; Di Grazia, M.; Finocchiaro, P.; Fronczek, F. R.; Mamo, A.; Pappalardo, S. Reaction of Tosylamide Monosodium Salt with Bis(halomethyl) Compounds: An Easy Entry to Symmetrical *N*-Tosyl Aza Macrocycles. *J. Org. Chem.* **1988**, *53*, 3521–9.
- (63) Pappalardo, S.; Bottino, F.; Di Grazia, M.; Finocchiaro, P.; Mamo, A. A Versatile One-Pot Synthesis of Symmetrical *N*-Tosylazamacrocycles. *Heterocycles* **1985**, *23* (8), 1881–4.
- (64) Wessel, A. J.; Schultz, J. W.; Tang, F.; Duan, H.; Mirica, L. M. Improved synthesis of symmetrically and asymmetrically *N*-substituted pyridinophane derivatives. *Org. Biomol. Chem.* **2017**, *15*, 9923–31.
- (65) Chessa, G.; Scrivanti, A. Synthesis of dendritic polypyridines with ethoxycarbonyl groups as surface functionality. *J. Chem. Soc., Perkin Trans. 1* **1996**, *1* (4), 307–311.
- (66) Alonso, E.; Ramon, D. J.; Yus, M. Reductive Deprotection of Allyl, Benzyl, and Sulfonyl Substituted Alcohols, Amines and Amides Using a Naphthalene-Catalysed Lithiation. *Tetrahedron* **1997**, *53* (42), 14355–68.
- (67) Wuts, P. G. M.; Greene, T. W. *Greene's Protective Groups in Organic Synthesis*, 4th ed.; John Wiley & Sons, Inc.: Hoboken, NJ, 2007.
- (68) Cabani, S.; Ceccanti, N.; Pardini, R.; Tiné, M. R. Thermodynamics and kinetics of dioxygen binding to Co(II) complexes with saturated macrocyclic tetraamines. *Polyhedron* **1999**, *18* (25), 3295–3303.
- (69) Tircso, G.; Regueiro-Figueroa, M.; Nagy, V.; Garda, Z.; Garai, T.; Kalman, F. K.; Esteban-Gomez, D.; Toth, E.; Platas-Iglesias, C. Approaching the Kinetic Inertness of Macrocyclic Gadolinium(III)-Based MRI Contrast Agents with Highly Rigid Open-Chain Derivatives. *Chem. - Eur. J.* **2016**, *22* (3), 896–901.
- (70) Cabani, S.; Ceccanti, N.; Pardini, R.; Tine, M. Thermodynamics and kinetics of dioxygen binding to Co(II) complexes with saturated macrocyclic tetraamines. *Polyhedron* **1999**, *18*, 3295–303.
- (71) Izatt, R. M.; Pawlak, K.; Bradshaw, J. S.; Bruening, R. L. Thermodynamic and kinetic data for macrocycle interactions with cations and anions. *Chem. Rev.* **1991**, *91*, 1721–85.
- (72) Di, L.; Kerns, E. H. Profiling drug-like properties in discovery research. *Curr. Opin. Chem. Biol.* **2003**, *7* (3), 402–408.
- (73) Levene, P. A.; Simms, H. S. Calculation of isoelectric points. *J. Biol. Chem.* **1923**, *55* (4), 801–813.
- (74) Tibbitts, J.; Canter, D.; Graff, R.; Smith, A.; Khawli, L. A. Key factors influencing ADME properties of therapeutic proteins: A need for ADME characterization in drug discovery and development. *mAbs* **2016**, *8* (2), 229–245.
- (75) Green, K. N.; Pota, K.; Tircso, G.; Gogolak, R. A.; Kinsinger, O.; Davda, C.; Blain, K.; Brewer, S.; Gonzalez, P.; Johnston, H. M.; Akkaraju, G. Dialing in on pharmacological features for a therapeutic antioxidant small molecule. *Dalton Trans.* **2019**, *48*, 12430.
- (76) Costa, J.; Delgado, R. Metal-Complexes of Macrocyclic Ligands Containing Pyridine. *Inorg. Chem.* **1993**, *32* (23), 5257–5265.
- (77) Savelieff, M. G.; Nam, G.; Kang, J.; Lee, H. J.; Lee, M.; Lim, M. H. Development of Multifunctional Molecules as Potential Therapeutic Candidates for Alzheimer's Disease, Parkinson's Disease, and Amyotrophic Lateral Sclerosis in the Last Decade. *Chem. Rev.* **2019**, *119* (2), 1221–1322.
- (78) Lincoln, K. M. Synthesis, Characterizations, and Applications of Pyridine- and Pyridol-Based Tetra-aza Macrocycles. Dissertation, Texas Christian University, Fort Worth, TX, 2015.
- (79) Lincoln, K. M.; Gonzalez, P.; Richardson, T. E.; Julovich, D. A.; Saunders, R.; Simpkins, J. W.; Green, K. N. A potent antioxidant small molecule aimed at targeting metal-based oxidative stress in neurodegenerative disorders. *Chem. Commun.* **2013**, *49* (26), 2712–4.

- (80) Safadi, M. E.; Bhadbhade, M.; Shimmon, R.; Baker, A. T.; McDonagh, A. M. Cyclen-based chelators for the inhibition of AB aggregation: Synthesis, anti-oxidant and aggregation evaluation. *Inorg. Chim. Acta* **2017**, *467*, 343–50.
- (81) Sharma, O. P.; Bhat, T. K. DPPH antioxidant assay revisited. *Food Chem.* **2009**, *113*, 1202–5.
- (82) Mao, F.; Yan, J.; Li, J.; Jia, X.; Miao, H.; Sun, Y.; Huang, L.; Li, X. New multi-target-directed small molecules against Alzheimer's disease: a combination of resveratrol and clioquinol. *Org. Biomol. Chem.* **2014**, *12* (31), 5936–44.
- (83) Storr, T.; Merkel, M.; Song-Zhao, G. X.; Scott, L. E.; Green, D. E.; Bowen, M. L.; Thompson, K. H.; Patrick, B. O.; Schugar, H. J.; Orvig, C. Synthesis, characterization, and metal coordinating ability of multifunctional carbohydrate-containing compounds for Alzheimer's therapy. *J. Am. Chem. Soc.* **2007**, *129* (23), 7453–7463.
- (84) Eckshtain-Levi, M.; Lavi, R.; Yufit, D. S.; Daniel, B.; Green, O.; Fleker, O.; Richman, M.; Rahimpour, S.; Gruzman, A.; Benisvy, L. A versatile water-soluble chelating and radical scavenging platform. *Chem. Commun.* **2016**, *52* (11), 2350–2353.
- (85) Galano, A.; Mazzone, G.; Alvarez-Diduk, R.; Marino, T.; Alvarez-Idaboy, J. R.; Russo, N. Food antioxidants: chemical insights at the molecular level. *Annu. Rev. Food Sci. Technol.* **2016**, *7*, 335–352.
- (86) Litwinienko, G.; Ingold, K. U. Abnormal Solvent Effects on Hydrogen Atom Abstractions. 1. The Reactions of Phenols with 2,2-Diphenyl-1-picrylhydrazyl (dpph•) in Alcohols. *J. Org. Chem.* **2003**, *68* (9), 3433–3438.
- (87) Nakanishi, I.; Kawashima, T.; Ohkubo, K.; Kanazawa, H.; Inami, K.; Mochizuki, M.; Fukuhara, K.; Okuda, H.; Ozawa, T.; Itoh, S.; Fukuzumi, S.; Ikota, N. Electron-transfer mechanism in radical-scavenging reactions by a vitamin E model in a protic medium. *Org. Biomol. Chem.* **2005**, *3* (4), 626–629.
- (88) Müller, L.; Fröhlich, K.; Böhm, V. Comparative antioxidant activities of carotenoids measured by ferric reducing antioxidant power (FRAP), ABTS bleaching assay ( $\alpha$ TEAC), DPPH assay and peroxy radical scavenging assay. *Food Chem.* **2011**, *129* (1), 139–148.
- (89) Méndez-Robles, M. D.; Permady, H. H.; Jaramillo-Flores, M. E.; Lugo-Cervantes, E. C.; Cardador-Martínez, A.; Canales-Aguirre, A. A.; López-Dellamary, F.; Cerda-García-Rojas, C. M.; Tamariz, J. C-26 and C-30 Apocarotenoids from Seeds of *Ditaxis h eterantha* with Antioxidant Activity and Protection against DNA Oxidative Damage. *J. Nat. Prod.* **2006**, *69* (8), 1140–1144.
- (90) Miller, N. J.; Sampson, J.; Candeias, L. P.; Bramley, P. M.; Rice-Evans, C. A. Antioxidant activities of carotenes and xanthophylls. *FEBS Lett.* **1996**, *384* (3), 240–242.
- (91) Adlard, P. A.; Bica, L.; White, A. R.; Nurjono, M.; Crouch, P. J.; Donnelly, P. S.; Cappai, R.; Finkelstein, D. I.; Bush, A. I.; Filiz, G. Metal ionophore treatment restores dendritic spin density and synaptic protein levels in a mouse model of Alzheimer's disease. *PLoS One* **2011**, *6* (3), No. e17669.
- (92) Andersen, J. K. Oxidative stress in neurodegeneration: cause or consequence? *Nat. Med.* **2004**, *10*, S18–25.
- (93) Gandhi, S.; Abramov, A. Y. Mechanism of Oxidative Stress in Neurodegeneration. *Oxid. Med. Cell. Longevity* **2012**, *2012*, 1–11.
- (94) Sayre, L. M.; Smith, M. A.; Perry, G. Chemistry and biochemistry of oxidative stress in neurodegenerative disease. *Curr. Med. Chem.* **2001**, *8* (7), 721–38.
- (95) Guilloreau, L.; Combalbert, S.; Sournia-Saquet, A.; Mazarguil, H.; Faller, P. Redox Chemistry of Copper-Amyloid-B: The Generation of Hydroxyl Radical in the Presence of Ascorbate is Linked to Redox-Potentials and Aggregation State. *ChemBioChem* **2007**, *8*, 1317–25.
- (96) Yepremyan, A.; Mehmood, A.; Brewer, S. M.; Barnett, M. M.; Janesko, B. G.; Akkaraju, G.; Simanek, E. E.; Green, K. N. A new triazine bearing a pyrazolone group capable of copper, nickel, and zinc chelation. *RSC Adv.* **2018**, *8*, 3024–35.
- (97) Faller, P.; Hureau, C.; Dorlet, P.; Hellwig, P.; Coppel, Y.; Collin, F.; Alies, B. Methods and techniques to study the bioinorganic chemistry of metal–peptide complexes linked to neurodegenerative diseases. *Coord. Chem. Rev.* **2012**, *256* (19–20), 2381–2396.
- (98) Vedernikov, A. N.; Wu, P.; Huffman, J. C.; Caulton, K. G. Cu(I) and Cu(II) complexes of a pyridine-based pincer ligand. *Inorg. Chim. Acta* **2002**, *330*, 103–110.
- (99) Lincoln, K. M.; Offutt, M. E.; Hayden, T. D.; Saunders, R. E.; Green, K. N. Structural, Spectral, and Electrochemical Properties of Nickel(II), Copper(II), and Zinc(II) Complexes Containing 12-Membered Pyridine- and Pyridol-Based Tetra-aza Macrocycles. *Inorg. Chem.* **2014**, *53* (3), 1406–1416.
- (100) Giulian, D. Microglia and the immune pathology of Alzheimer disease. *Am. J. Hum. Genet.* **1999**, *65* (1), 13–18.
- (101) Stansley, B.; Post, J.; Hensley, K. A comparative review of cell culture systems for the study of microglial biology in Alzheimer's disease. *J. Neuroinflammation* **2012**, *9* (1), 115.
- (102) Fleisher-Berkovich, S.; Filipovich-Rimon, T.; Ben-Shmuel, S.; Hülsmann, C.; Kummer, M. P.; Heneka, M. T. Distinct modulation of microglial amyloid  $\beta$  phagocytosis and migration by neuropeptides i. *J. Neuroinflammation* **2010**, *7* (1), 61.
- (103) Maezawa, I.; Zimin, P. I.; Wulff, H.; Jin, L.-W. Amyloid- $\beta$  protein oligomer at low nanomolar concentrations activates microglia and induces microglial neurotoxicity. *J. Biol. Chem.* **2011**, *286* (5), 3693–3706.
- (104) Masimirembwa, C. M.; Bredberg, U.; Andersson, T. B. Metabolic stability for drug discovery and development - Pharmacokinetic and biochemical challenges. *Clin. Pharmacokinet.* **2003**, *42* (6), 515–528.
- (105) Kwon, Y. *Handbook of Essential Pharmacokinetics, Pharmacodynamics and Drug Metabolism for Industrial Scientists*; Kluwer Academic/Plenum Publishers: New York, 2001.
- (106) Schlichting, I.; Berendzen, J.; Chu, K.; Stock, A. M.; Maves, S. A.; Benson, D. E.; Sweet, R. M.; Ringe, D.; Petsko, G. A.; Sligar, S. G. The Catalytic Pathway of Cytochrome P450cam at Atomic Resolution. *Science* **2000**, *287* (5458), 1615–1622.
- (107) Guengerich, F. P. Common and Uncommon Cytochrome P450 Reactions Related to Metabolism and Chemical Toxicity. *Chem. Res. Toxicol.* **2001**, *14* (6), 611–650.
- (108) Obach, R. S. Prediction of human clearance of twenty-nine drugs from hepatic microsomal intrinsic clearance data: An examination of in vitro half-life approach and nonspecific binding to microsomes. *Drug Metab. Dispos.* **1999**, *27* (11), 1350–1359.
- (109) McNaney, C. A.; Drexler, D. M.; Hnatyshyn, S. Y.; Zvyaga, T. A.; Knipe, J. O.; Belcastro, J. V.; Sanders, M. An automated liquid chromatography-mass spectrometry process to determine metabolic stability half-life and intrinsic clearance of drug candidates by substrate depletion. *Assay Drug Dev. Technol.* **2008**, *6* (1), 121–129.
- (110) Williamson, B.; Wilson, C.; Dagnell, G.; Riley, R. J. Harmonised high throughput microsomal stability assay. *J. Pharmacol. Toxicol. Methods* **2017**, *84*, 31–36.
- (111) It's Time for Pharmaceutical Companies to Have Their Tobacco Moment. *New York Times*; **2019**; p 22; February 24.
- (112) Pollack, A. Drug Goes From \$13.50 a Tablet to \$750, Overnight. *New York Times*; **2015**; p 2015, September 21.
- (113) Berger, O.; Winters, K. R.; Sabourin, A.; Dzyuba, S. V.; Montchamp, J.-L. On the cost of academic methodologies. *Org. Chem. Front.* **2019**, *6* (12), 2095–2108.
- (114) Nikac, M.; Brimble, M. A.; Crumbie, R. L. Synthesis of thiacycrown and azacycrown ethers based on a spiroacetal framework. *Tetrahedron* **2007**, *63* (24), 5220–6.
- (115) Favre-Reguillon, A.; Segat-Dioury, F.; Nait-Bouda, L.; Cosma, C.; Siaugue, J. M.; Foos, J.; Guy, A. A Highly Chemoselective Protection and Activation of Primary Amines in Polyamine. *Synlett* **2000**, No. 6, 868–70.
- (116) Irving, H. M.; Miles, M. G.; Pettit, L. D. A Study of Some Problems in Determining the Stoichiometric Proton Dissociation Constants of Complexes by Potentiometric Titrations Using a Glass Electrode. *Anal. Chim. Acta* **1967**, *38*, 475–488.
- (117) Zekany, L.; Nagypal, I. PSEQUAD. In *Computational Methods for the Determination of Formation Constants*; Leggett, D. J., Ed.; Springer: Boston, MA, 1985; pp 291–353.

(118) Delgado, R.; Da Silva, J. F.; Amorim, M.; Cabral, M.; Chaves, S.; Costa, J. Dissociation constants of Brønsted acids in D<sub>2</sub>O and H<sub>2</sub>O: studies on polyaza and polyoxa-polyaza macrocycles and a general correlation. *Anal. Chim. Acta* **1991**, *245*, 271–282.

(119) APEX3, version 1; Bruker AXS Inc.: Madison, WI, 2016.

(120) SAINT; Bruker AXS Inc.: Madison, WI, 2012.

(121) SADABS; Bruker AXS Inc.: Madison, WI, 2001.

(122) Dolomanov, O. V.; Bourhis, L. J.; Gildea, R. J.; Howard, J. A. K.; Puschmann, H. OLEX2: a complete structure solution, refinement and analysis program. *J. Appl. Crystallogr.* **2009**, *42*, 339–41.

(123) Sheldrick, G. M. A short history of SHELX. *Acta Crystallogr., Sect. A: Found. Crystallogr.* **2008**, *A64*, 112–22.

(124) Sheldrick, G. M. Crystal structure refinement with SHELXL. *Acta Crystallogr., Sect. C: Struct. Chem.* **2015**, *C71*, 3–8.

(125) Faller, P.; Hureau, C.; Dorlet, P.; Hellwig, P.; Coppel, Y.; Collin, F.; Alies, B. Methods and techniques to study the bioinorganic chemistry of metal-peptide complexes linked to neurodegenerative diseases. *Coord. Chem. Rev.* **2012**, *256*, 2381–96.

(126) Houston, J. B. Utility of in-Vitro Drug-Metabolism Data in Predicting in-Vivo Metabolic-Clearance. *Biochem. Pharmacol.* **1994**, *47* (9), 1469–1479.

(127) Davies, B.; Morris, T. Physiological parameters in laboratory animals and humans. *Pharm. Res.* **1993**, *10* (7), 1093–1095.

(128) Barter, Z. E.; Bayliss, M. K.; Beaune, P. H.; Boobis, A. R.; Carlile, D. J.; Edwards, R. J.; Brian Houston, J.; Lake, B. G.; Lipscomb, J. C.; Pelkonen, O. R.; Tucke, G.; Rostami-Hodjegan, A. Scaling factors for the extrapolation of in vivo metabolic drug clearance from in vitro data: reaching a consensus on values of human micro-somal protein and hepatocellularity per gram of liver. *Curr. Drug Metab.* **2007**, *8* (1), 33–45.

(129) Iwatsubo, T.; Suzuki, H.; Sugiyama, Y. Prediction of species differences (rats, dogs, humans) in their in vivo metabolic clearance of YM796 by the liver from in vitro data. *J. Pharmacol. Exp. Ther.* **1997**, *283* (2), 462–469.